NASA/TM—1998-208403

Vortex/Body Interaction and Sound Generation in Low-Speed Flow

Hsiao C. Kao
Lewis Research Center, Cleveland, Ohio

National Aeronautics and
Space Administration

Lewis Research Center

September 1998

Available from

NASA Center for Aerospace Information
7121 Standard Drive
Hanover, MD 21076
Price Code: A03

National Technical Information Service
5287 Port Royal Road
Springfield, VA 22100
Price Code: A03

VORTEX/BODY INTERACTION AND SOUND GENERATION IN LOW-SPEED FLOW

Hsiao C. Kao
National Aeronautics and Space Administration
Lewis Research Center
Cleveland, Ohio 44135

SUMMARY

The problem of sound generation by vortices interacting with an arbitrary body in a low-speed flow has been investigated by the method of matched asymptotic expansions. For the purpose of this report, it is convenient to divide the problem into three parts. In the first part the mechanism of the vortex/body interaction, which is essentially the inner solution in the inner region, is examined. The trajectories for a system of vortices rotating about their centroid are found to undergo enormous changes after interaction; from this, some interesting properties emerged. In the second part, the problem is formulated, the outer solution is found, matching is implemented, and solutions for acoustic pressure are obtained. In the third part, Fourier integrals are evaluated and predicated results presented. An examination of these results reveals the following: (a) the background noise can be either augmented or attenuated by a body after interaction, (b) sound generated by vortex/body interaction obeys a scaling factor, (c) sound intensity can be reduced substantially by positioning the vortex system in the "favorable" side of the body instead of the "unfavorable" side, and (d) acoustic radiation from vortex/bluff-body interaction is less than that from vortex/airfoil interaction under most circumstances.

1. INTRODUCTION

Since the pioneer work of Lighthill, many theories and numerical methods for predicting aeroacoustics have been put forward. Most of these theories involve volume or surface integrals to account for source distributions in the turbulent near field. However, since a quantitative description of turbulent flows is difficult, perhaps we can, from a practical point of view, justify exploring some simpler methods.

The aerodynamic aspect of sound production is known to be characterized by the formation of eddy motions (see Powell's formulation of vortex sound in ref. 1 or 2). A simplified representation of these motions is the singular distribution of vorticity, such as the discrete vortices moving in an inviscid fluid. The justification for this can be found elsewhere (e.g., ref. 3); however, a brief description is provided here.

In a viscous fluid and at a relatively low Reynolds number, the velocity and vorticity fields are usually continuous. As the Reynolds number increases, the vorticity field becomes more concentrated and is often embedded in an otherwise irrotational flow field. In taking the limit, these concentrated vorticity fields, which are governed by the Biot-Savort law, may then be modeled by discrete vortices with given circulations. The discovery of large-scale coherent structures in turbulent flows, especially in mixing layers, provides a further justification for this model. Considerable numerical work has been done in the application of various forms of discrete vortex methods to simulate two-dimensional mixing layers (e.g., ref. 4).

Because of a great increase in computing speed, aeroacoustics computations based on the unsteady Euler or Navier-Stokes equations can now be performed. However, obtaining accurate solutions depends on the resolution of certain issues, such as the size of the computational domain, the outer boundary conditions, and such. Thus far, no satisfactory solutions for these issues have been attained (ref. 5).

Notwithstanding these problems, computational aeroacoustics may still be the most promising method in the long run. At present, the use of simpler methods without these problems may be justified. To this end, one chooses a potential flow model with discrete vortices to represent the flow in the inner region. And it is known that "all acoustic motions in the vicinity of a singularity are solutions of Laplace's equation" (p. 40, ref. 6). To solve acoustic problems, the solution in the potential flow region has to be matched to the outer solution of the compressible flow (acoustic field) by means of the method of matched asymptotic expansion. The acoustic equation to be used herein is the acoustic equation for a moving medium instead of that for a stationary medium.

The problem now has been separated into two parts: an inner potential flow region and an outer acoustic field. This enables us to deal with complex geometries for the following two reasons. (a) There are a number of numerical methods available for two-dimensional potential flow in the presence of arbitrary bodies. The method used here is based on Martensen's formulation and is that favored mostly by British researchers (e.g., see ref. 7 or 8). The advantage of this method for the present problem is that a body is replaced by a distribution of surface vorticity elements. Thus, the surface and the moving vortices can be treated similarly by the same Biot-Savart law. (b) The detailed flow characteristics of the inner region in an acoustically compact region will not, in general, affect aeroacoustics. Instead, only the gross properties of the potential flow influence the acoustic radiation. The evidence for this is that after a Fourier transform has been taken, the acoustic equation becomes a Bessel equation whose solution for the outgoing wave is a Hankel function. Thus, the solution for sound radiation in the frequency domain is nearly determined. The matching process merely determines the coefficients. For this reason, even for a body of very complex geometry, once the inner solution is known, the pressure fluctuation in the far field in the frequency domain is established.

The idea of using asymptotic matching to study aeroacoustics in a low-speed flow has been implemented in the past (e.g., refs. 9 to 15). In these studies if a body was present, it was usually of a simple shape, so the method of conformal mapping was applicable. Here we propose to broaden this method to include an arbitrary body and to adopt the acoustic equation in a moving medium.

Although the outer solution is known in the frequency domain, an inverse Fourier transform is still necessary to bring it back to the physical domain. This has to be done numerically for a general case. There are at least two methods available. One is the method of the discrete Fourier transform, and the other is the method of convolution integral. The former is well known and its application to the present problem is relatively straightforward. The latter involves divergent integrals, which were derived by Conlisk and coworkers (ref. 13 and related papers), but which have not been evaluated numerically for far-field acoustic pressure fluctuations. Let us re-examine this method to see why divergent integrals appear, and to evaluate these integrals with the help of Hadamard's (ref. 16) definition of the final part.

This study examines sound generation by a vortex/body interaction. Initially a group of spinning vortices (see fig. 1) is introduced at an upstream station; as they move downstream and pass near the surface, an interaction takes place. This interaction causes the vortex trajectories to deviate from their original paths, alters the characteristics of the background noise, and gives rise to sound radiation. We studied each of these aspects in some detail and present the results herein.

The results of this investigation are presented in the following sections. In sections 2 and 3, respectively, we derive the potential flow solutions in the inner region and discuss the related topics of vortex trajectories and their interaction with the body. In section 4, a brief description of the formulation is given, which leads to the Fourier transform of the inner solutions in section 5 and the outer solutions in the frequency domain in section 6. Section 7 considers the process of matching and the solution for the acoustic pressure. Sections 8 to 10 cover two methods for evaluating the Fourier integrals and the test cases for the background noise. In section 11 results are presented and discussed.

SYMBOLS

$\bar{c}$	airfoil chord length
ds_m	length of surface element at point s_m
K	influence coefficient
M	total number of surface elements
M_0	free-stream Mach number
N	total number of free vortices
p'	fluctuating (acoustic) pressure
R	radial coordinate in outer region

r'	radial coordinate in inner region
s	position of surface element
t	time in moving frame
U_0	free-stream velocity
u,v	velocity components in x and y directions
u_s	surface velocity
W	complex potential
x,y	Cartesian coordinates
$z = x + iy$	complex number
z_{ct}	initial position of vortex centroid
β	radius of spinning vortices
Γ	strength of vortex
γ_m	surface vorticity per unit length at point s_m
δ_m	radial coordinate of surface element s_m
θ	angular coordinate of observation point
θ'	angular coordinate in inner and outer regions
θ_m, θ_n	angular coordinate of surface element m or n
τ	time in fixed frame
Φ	velocity potential
Ψ	stream function
$\overline{\Omega}$	angular velocity of spinning vortices
ω	angular frequency in Fourier transform
ω_0	frequency of spinning vortices

Subscript

i	ith free vortex
m,n	surface element (point) m,n
0	initial position or free-stream condition

2. POTENTIAL FLOW SOLUTIONS IN THE INNER REGION

As stated previously, an incompressible potential flow is assumed to exist in the inner region, which includes a body as well as the moving rectilinear vortices with constant circulations concentrated at the singularities. The complex potential $\overline{W}$ for an isolated vortex located at $\bar{z}_0$ in a free space is

$$\overline{W} = \overline{\Phi} + i\overline{\Psi} = \frac{i\overline{\Gamma}}{2\pi}\log(\bar{z} - \bar{z}_0) \tag{1}$$

where $\overline{\Phi}$ is the velocity potential; $\overline{\Psi}$ is the stream function; $\overline{\Gamma}$ is the circulation defined to be positive in the clockwise direction; $\bar{z} = \bar{x} + i\bar{y}$; and $\bar{z} = \bar{x} + i\bar{y}$. This is the building block for the potential flow to be discussed.

Our present interest is to study the interaction of vortices with a body in a stream and, therefore, the presence of the body has to be taken into account. First, we consider Martensen's method of potential flow calculation for a body of arbitrary shape without the moving vortices (for more details, see either of Martensen's papers, or ref. 7 or 8.) Since Martensen's method is not based on a transformation method, no images of vortices are necessary. The body is defined by a string of surface vorticity elements separating the moving stream outside the body from a stationary medium inside the body. The complex potential is simply a summation of M surface vorticity elements of undetermined strength, denoted as γ_m, plus the uniform free stream:

$$W = \Phi + i\Psi = \sum_{m=1}^{M} \frac{i\gamma_m ds_m}{2\pi}\log(z - z_m) + z \tag{2}$$

Symbols here denote dimensionless quantities and are defined as follows:

$$W = \overline{W}/\overline{U}_0\bar{l}, \quad z = \bar{z}/\bar{l}, \quad \gamma_m = \bar{\gamma}_m/\overline{U}_0, \quad ds_m = \Delta\bar{s}_m/\bar{l}$$

where $\overline{U}_0$ is the free-stream velocity; $\bar{l}$ is the reference length; $\bar{\gamma}_m$ is the surface vorticity per unit length located at the point $\bar{z}_m$ on the surface of the body; and $\Delta\bar{s}_m$ is the length of the element (see fig. 2). (In subsequent calculations, the reference length for an airfoil is the chord and that for a rectangular block is the height.) The last term in equation (2) is the complex potential for the uniform free stream assumed to be parallel to the x-axis. It follows that

$$\frac{dW}{dz} = u - iv = \sum_{m=1}^{M} \frac{i\gamma_m ds_m}{2\pi}\frac{1}{z - z_m} + 1$$

$$u(x,y) = \sum_{m=1}^{M} \frac{\gamma_m ds_m}{2\pi}\frac{y - y_m}{(x - x_m)^2 + (y - y_m)^2} + 1 \tag{3}$$

$$v(x,y) = -\sum_{m=1}^{M} \frac{\gamma_m ds_m}{2\pi}\frac{x - x_m}{(x - x_m)^2 + (y - y_m)^2}$$

The symbols u and v denote the velocity components in the x- and y-directions at a point x and y in the space induced by M surface vorticity elements. To determine the unknown γ_m in equation (2), we apply equation (3) at the surface elements s_n and impose the Dirichlet condition that the internal tangential velocity component is zero:

$$\frac{1}{2\pi}\sum_{m=1,n\neq m}^{M}\gamma_m ds_m K(s_n,s_m)+\gamma_n\left(\frac{1}{4\pi}\frac{ds_n}{R_n}-\frac{1}{2}\right)=-\cos\theta_n,\qquad n=1,2,\ldots,M \tag{4}$$

$$K(s_n,s_m)=\frac{(y_n-y_m)\cos\theta_n-(x_n-x_m)\sin\theta_n}{(x_n-x_m)^2+(y_n-y_m)^2}$$

Here x_n, y_n are the coordinates for s_n; R_n is the radius of curvature at s_n; θ_n is the tangential angle at s_n (see fig. 2); and $K(s_n, s_m)$ is the influence coefficient, which represents the tangential velocity component induced at s_n by other surface vorticity elements. The second term on the left side of the equation refers to the self-induced velocity of vortex element $\gamma_n ds_n$.

Equation (4) is a system of M simultaneous equations for M unknowns γ_m. The potential flow problem for the inner region is now reduced to the solution of M linear simultaneous equations. Any standard method can be used to solve it, for there is no ill-conditioning involved. We have used the Gaussian elimination method for every calculation performed so far.

The accuracy of this method has been assessed by Lewis (ref. 7), who compared its results with the known exact solutions, including those for bodies with sharp corners. We have also done our own comparisons, with such configurations as the NACA 0012 airfoil, and like Lewis, we concluded that we have a "high level of confidence" in this method. (For a cusped airfoil the accuracy may deteriorate.) Plotted in figure 3 is the velocity distribution at the forward corner of a sharp-edged rectangular block in a uniform flow. This is an indirect comparison since as the length increases, the potential flow at the sharp corner approaches that of a step for which the exact solution exists. The 2:1 ratio rectangle can almost simulate a step. Also plotted in figure 3 is the surface velocity distribution in the forward face of the same rectangle but with round-edged corners. Both of these configurations will be used later for predicting sound generation, and we will see that even slight rounding of the corners can reduce sound radiation.

Let us now consider the problem of vortex/body interaction. With the presence of free vortices in the field, equation (4) assumes a somewhat different form:

$$\frac{1}{2\pi}\sum_{m=1,m\neq n}^{M}\gamma_m ds_m K(s_n,s_m)+\gamma_n\left(\frac{ds_n}{4\pi R_n}-\frac{1}{2}\right)=-\cos\theta_n-\frac{1}{2\pi}\sum_{i=1}^{N}\Gamma_i K(s_n,z_i) \tag{5}$$

The last term on the right side of this equation accounts for the presence of the N free vortices, whose influence coefficient assumes the form

$$K(s_n,z_i)=\frac{(y_n-y_i)\cos\theta_n-(x_n-x_i)\sin\theta_n}{(x_n-x_i)^2+(y_n-y_i)^2}$$

A two-dimensional vortex induces no velocity at its own center and moves with the local free-stream velocity plus the velocities induced by the other vortices. With the presence of these free vortices Γ_i, equation (3) becomes

$$u_j-iv_j=\sum_{m=1}^{M}\frac{i\gamma_m ds_m}{2\pi}\frac{1}{z_j-z_m}+1+\sum_{i=1,i\neq j}^{N}\frac{i\Gamma_i}{2\pi}\frac{1}{z_j-z_i} \tag{6}$$

where z_j is the coordinate for vortex j, and u_j, v_j are the velocity components at z_j. Here z_i and γ_m are functions of time, but ds_m, z_m, and Γ_i are constants.

The evolution of vortex j is governed at each time step by the following two first-order differential equations:

$$\frac{dx_j}{d\tau} = u_j, \qquad \frac{dy_j}{d\tau} = v_j \tag{7}$$

For a field with N vortices there are $2N$ such equations whose solutions give the trajectories for N vortices. At each time step, we have to update γ_m, by solving equation (5). A second-order method is used for computing the time development from τ to $\tau + \Delta\tau$:

$$x_j(\tau + \Delta\tau) = x_j(\tau) + \frac{1}{2}\left[3u_j(\tau) - u_j(\tau - \Delta\tau)\right]\Delta\tau$$

$$y_j(\tau + \Delta\tau) = y_j(\tau) + \frac{1}{2}\left[3v_j(\tau) - v_j(\tau - \Delta\tau)\right]\Delta\tau$$

The time step $\Delta\tau$ is generally determined by comparing two solutions, one obtained with $\Delta\tau$ and the other with $\Delta\tau/2$. If these two solutions agree reasonably well, the time step $\Delta\tau$ is chosen; otherwise the process continues. In general, $\Delta\tau = 0.0125$ to 0.025 was found to be acceptable. The initial conditions for equation (7) are the coordinates of free vortices at locations sufficiently far upstream, where the interaction with the body is minimal.

The accuracy of this method for a single free vortex was assessed by comparing two trajectories past a circular cylinder in an incompressible flow; one was obtained by the present method and the other was the exact solution obtained by the image method. In a test run with $\Delta\tau = 0.1$ and $\Gamma = -1.0$, four-figure accuracy was attained in the vortex position, except very near the surface of the body, where the accuracy was reduced to three figures.

3. VORTEX TRAJECTORIES AND INTERACTIONS

With the necessary equations for a potential flow in place, we can now proceed with the solutions. First, a few remarks are in order.

Three conservation laws apply to a system of discrete vortices in a two-dimensional unbounded fluid at rest at infinity; one of these states that the centroid of the system is stationary. If there are N equal, like-signed vortices spaced equally around the circumference of a circle, they rotate about the centroid with a constant angular velocity. In the present study N is equal to 4 or less. Emphasis will, however, be placed on a pair of spinning vortices, since this is a classical example for acoustic radiation and there is an analytic solution for it. When such a system is placed in a moving stream, the centroid moves with the local convective velocity.

The central topics of the present investigation are the vortex trajectory patterns and the acoustic radiation from the interaction. Problems of a similar nature have been previously studied. For example, Hardin and Mason (ref. 17) examined the blade/vortex interaction for a single vortex and the associated sound generation. Their results will be used later for comparison with the present solutions. More recently, Panaras (ref. 18) investigated the vortex trajectories for many vortices and their interactions with several Joukowski airfoils. However, the relatively large number of vortices used in the investigation may have obscured the process, since the vortices developed irregular patterns prior to the interaction. As a result, the effect of the interaction on the vortex trajectories cannot be easily seen.

In order to see the effect of an interaction, it is preferable to limit the vortices to a small number and to arrange them in such a way that the motion prior to interaction is regular; thus, the change in their trajectories can be discerned immediately. To this end, the present system consists of no more than four vortices, and it undergoes a circular motion in a stationary medium. With the convective velocity included, the trajectory of each individual vortex forms a wave pattern (figs. 4 to 9).

Hardin and Mason pointed out that vortex/blade interactions are highly nonlinear, which is also true here. So a slight change in the initial conditions may result in distinctly different trajectories after interaction. For this reason a number of plots are included here to show the different possibilities that an interaction can bring. In figure 4 three trajectories by a pair of spinning vortices of equal and positive strength (clockwise rotation) are shown. Initially this pair was stacked in an upstream station (fig. 1), whose vertical distances measured from the airfoil chord line are the same, but the horizontal distances from the leading edge of the airfoil are different. With $x_1 = x_2 = -24.4$, the fore and aft trajectories are similar. However, as the initial position of the pair moves forward to –24.6 (20 percent of the

chord), the trajectories after interaction (the aft trajectories) are no longer the same as the upstream trajectories (the fore trajectories). The pair spins faster behind the airfoil. If the pair moves further upstream to –25.0, a pronounced change in the aft trajectory pattern takes place, in which case the vortices depart from each other and, consequently, the rotating speed becomes much smaller. This suggests that the background noise of a spinning vortex pair can be attenuated by interaction with a body, which we will examine later. To understand this scenario, we cite a well-known equation given in reference 19:

$$\overline{\Omega} = \frac{1}{4\pi \bar{a}^2}(N-1)\overline{\Gamma} \tag{8}$$

where $\overline{\Omega}$ is the angular velocity and N represents N equal, like-signed vortices $\overline{\Gamma}$ arranged uniformly about a circle of radius $\bar{a}$. According to this equation, the spin rate becomes smaller as the two vortices depart from each other, and the associated sound decreases.

A closer examination of the trajectories reveals that here the aft trajectory patterns are periodic in the sense that their evolution from a high to a low rotating rate repeats itself as the initial position of the vortex pair is repositioned continuously forward or backward. The reason for this is that a vortex moves along a wavy path and its time of arrival in the neighborhood of the airfoil is periodic.

Thus far, only the positive vortices placed above the chord line have been studied. If they are replaced by two negative (counterclockwise) vortices with the other conditions unchanged, the fore and aft trajectories of all three previously mentioned cases become similar. For example, figure 5 is a counterpart of figure 4(c), with identical parameters except for the sense of the vortices. In reference 14, Sen quotes Howe's result that a vortex produces sound mainly when it cuts across base streamlines near an edge. The velocity field induced by a negative vortex is in the direction of the local (base) convective velocity and, therefore, produces less disturbance. By contrast, the velocity field induced by a positive vortex goes against the local convective velocity near the surface, so the vortices are more likely to be repelled to a different orbit. On the basis of this intuitive notion, we would expect a pair of positive vortices placed below the chord line to have the same effect as a pair of negative vortices above the chord line. This expectation turned out to be correct and has been verified by calculations.

Three different trajectory patterns are shown in figure 6, one of which involves four vortices. They are included here because these patterns will be used later to calculate acoustic pressures. Note that the bluff body (a 2:1 ratio block) shown in figure 6(b) and the following figures is merely a distorted schematic of the real geometry. Since there is a large disparity between the vertical and horizontal scale, a 2:1 block would be unrecognizable if plotted to scale.

Apparently this intuitive notion for an airfoil is also applicable to the vortex/bluff-body interaction. For example, see figure 7, where two sets of trajectories for a sharp-edged bluff body are plotted. Again, the initial conditions for parts (a) and (b) of figure 7 are the same; only the sense of the vortices is different.

Previously, we dealt exclusively with equal and like-signed vortices. If we ease this constraint a little to permit vortices of unequal strengths, the centroid will be shifted to one side; other aspects of the trajectory pattern will, however, remain essentially the same. For this reason, no results and graphics have been included.

Let us now shift our attention to the interactions involving three like-signed vortices of equal strength rotating at a constant speed (fig. 1). In this case the forward trajectories are essentially three intertwined identical curves, but the aft trajectories are a variety of vastly different patterns. Consequently, only a representative case is shown in figure 8, which consists of two sets of curves, one for a sharp-edged body and the other for an equivalent round-edged body. The purpose is to demonstrate the influence of a corner. Apparently, rounding off the corners slightly can make a difference in the aft pattern as well as in the acoustic radiation.

Usually, after a vortex/body interaction, the trajectories become less organized, as can be seen in the aforementioned figures. The reverse may also be true in the sense that after an interaction vortices may spin in a more orderly fashion than before. This possibility is depicted in figure 9, which shows all three aft vortices rotating at nearly the same speed.

4. FORMULATION

The problem to be considered consists of two regions: an inner and an outer region. The governing equations for the former have been given. In this section the differential equations for the latter are to be derived. Since the

acoustic pressure radiated from a source will be distorted after traveling through a convective stream, it is preferable to find solutions based on the acoustic equation in a moving medium instead of in the stationary medium used in earlier investigations. This equation for a fixed frame of reference is given by

$$\frac{\partial^2 p'}{\partial x^2}+\frac{\partial^2 p'}{\partial y^2}-M_0^2\frac{D^2 p'}{D\tau^2}=0, \quad \text{where} \quad \frac{D}{D\tau}=\frac{\partial}{\partial \tau}+\frac{\partial}{\partial x} \tag{9}$$

The symbols p', τ, x, y, M_0 are, respectively, the dimensionless quantities for the perturbed pressure, time, spatial coordinates, and Mach number. They are defined as follows:

$$p'=\frac{\bar{p}'}{\bar{\rho}_0\bar{U}_0^2}, \quad \tau=\frac{\bar{U}_0\bar{t}}{\bar{l}}, \quad x=\frac{\bar{x}}{\bar{l}}, \quad y=\frac{\bar{y}}{\bar{l}}, \quad M_0=\frac{\bar{U}_0}{\bar{c}_0}$$

where $\bar{\rho}_0$ is the density, $\bar{l}$ is the reference length, t is time, and $\bar{c}_0$ is the speed of sound. To make the analysis more tractable, this equation is transformed from a fixed frame to a moving coordinate system (ref. 20) by defining $x' = x - \tau$, $y' = y$, and $t = \tau$. Thus,

$$\frac{\partial^2 p'}{\partial x'^2}+\frac{\partial^2 p'}{\partial y'^2}-M_0^2\frac{\partial^2 p'}{\partial t^2}=0 \tag{10}$$

This equation is of the same form as the classical acoustic equation. Therefore, all available methods for solving the classical equation can now be put to use. Once the solution is known, it can be transformed back to the fixed frame of reference.

Introducing two outer variables defined as $R = M_0 r'$ and $\theta' = \tan^{-1} y'/x'$, where $r' = (x'^2 + y'^2)^{1/2}$, we obtain

$$\frac{\partial^2 p'}{\partial R^2}+\frac{1}{R}\frac{\partial p'}{\partial R}+\frac{1}{R^2}\frac{\partial^2 p'}{\partial \theta'^2}-\frac{\partial^2 p'}{\partial t'^2}=0 \tag{11}$$

This is the final form of the governing equation for the outer region, subject to the radiation condition at infinity and asymptotic matching near the body.

On the basis of the premise that steady flows generate no sound, the inner potential flow equations and the subsequent numerical expressions can be written in such a way that the unsteady part is separated from the steady part. For the purpose of matching, we have to express the unsteady velocity potential in terms of p' given by the linearized Bernoulli equation:

$$p' = p - p_0 = -\frac{D\Phi'}{D\tau}=\frac{\partial \Phi'}{\partial t} \tag{12}$$

The operator $D/D\tau$ represents the time rate of change of Φ' as seen by an observer moving with the free-stream velocity. Note that the notation τ denotes time in a fixed frame. If a moving frame is used, τ will become t and $D\Phi'/D\tau$ becomes $\partial\Phi'/\partial t$.

5. FOURIER TRANSFORM OF INNER SOLUTION

With the governing equations for the inner and outer regions both attained, we can proceed to solve low-speed aeroacoustics problems. As briefly mentioned in section 1, the procedure is as follows. First the unsteady part of the inner solution in the limit as $r \to \infty$ is determined, from which, by means of equation (12), the perturbation pressure p' is found. Next, the Fourier transform of p' is obtained for matching. The partial differential equation (eq. (11)), is

then transformed via the Fourier transform to an equivalent ordinary differential (Bessel) equation, whose solution for the outgoing wave at infinity in the frequency domain is the Hankel function. The limiting form of this function as $R \to 0$ is matched to the inner solution to secure the unknown coefficients. Then in the last step, an inverse transform is performed to return the solution to the physical space.

Following these steps, let us proceed to determine the inner solution by first considering a pair of spinning vortices moving past a body. The complex potential for this system is similar to that of equation (2):

$$W = \Phi + i\Psi = \sum_{m=1}^{M} \frac{i\gamma_m ds_m}{2\pi} \log(z - z_m) + z + \frac{i\Gamma}{2\pi} \log\left[z - (\tau + z_{ct} + z_0 + z_1)\right] + \frac{i\Gamma}{2\pi} \log\left[z - (\tau + z_{ct} - z_0 + z_2)\right] \quad (13)$$

Most symbols in this equation have been previously defined. The terms in the last two sets of brackets represent the positions of the spinning pair. The symbol z_{ct} refers to the initial position of the vortex centroid and is a constant. The quantity $\tau + z_{ct}$ is the position of the centroid at time τ convected by the free stream in the absence of a body. The symbols $\pm z_0$ are the local coordinates of vortices relative to the centroid (fig. 1). If the body is absent, this pair rotate freely, are always aligned, and need only the quantities $\tau + z_{ct} \pm z_0$ to denote their instantaneous positions. However, in the presence of a body, these positions will be perturbed because of the interaction with the body; thus we introduce z_1 and z_2.

After excluding the steady part in equation (13), the relevant portion is the unsteady part W' given by

$$W' = \sum_{m=1}^{M} \frac{i\gamma_m ds_m}{2\pi} \log\left[z\left(1 - \frac{z_m}{z}\right)\right] + \frac{i\Gamma}{2\pi}\left[\log\left(1 - \frac{z_0 + z_1}{z - \tau - z_{ct}}\right) + \log\left(1 + \frac{z_0 - z_2}{z - \tau - z_{ct}}\right)\right]$$

Expanding this equation for $|z_m/z| << 1$, $|(z_0 + z_1)/(z - \tau - z_{ct})| << 1$, $|(z_0 - z_2)/(z - \tau - z_{ct})| << 1$, and defining $z = r\exp(i\theta)$ and $z_m = \delta_m \exp(i\theta_m)$, we have

$$W' = \sum_{m=1}^{M} \frac{i\gamma_m ds_m}{2\pi}\left[\log r + i\theta - \frac{\delta_m}{r} e^{i(\theta_m - \theta)}\right] + \frac{i\Gamma}{2\pi}\left[-\frac{z_1}{(z - \tau - z_{ct})} - \frac{z_2}{(z - \tau - z_{ct})} - \frac{z_0^2}{(z - \tau - z_{ct})^2}\right] + \ldots \quad (14)$$

The first two terms in the first pair of brackets are zero, because $\sum_{m=1}^{M} \gamma_m ds_m = 0$. This is due to the fact that $\sum_{m=1}^{M} \gamma_m ds_m = \oint (\partial \Phi / \partial s) ds = 0$, provided that there is no circulation.[1] (γ_m can also denote the surface tangential velocity component; see ref. 7.) Note that only one second-order term in this equation is retained; others have been dropped. This second-order term represents the unsteady motion of the spin and produces the background noise. Other terms in this equation are first-order terms that are essentially zero until the vortices experience an interaction with the body, and they will return to zero after the interaction is over.

The next step is to put equation (14) in a more convenient form and then to find p' by means of equation (12). Introducing the polar coordinates of the following quantities,

$$z - \tau - z_{ct} = r' e^{i\theta'} \quad \text{and} \quad z_0 = \beta e^{i\omega_0 t}$$

where $\omega_0 = \Gamma/4\pi\beta^2$, we transform equation (14) to the form

$$W' = \Phi' + i\Psi' = -i \sum_{m=1}^{M} \frac{\gamma_m ds_m}{2\pi} \frac{\delta_m}{r} e^{i(\theta_m - \theta)} - \frac{i\Gamma}{2\pi} \frac{x_1 + iy_1 + x_2 + iy_2}{r'} e^{-i\theta'} - \frac{i\Gamma}{2\pi} \frac{\beta^2}{r'^2} e^{2i(\omega_0 t - \theta')} \quad (15)$$

[1] If there is a strong vortex system in the proximity of a symmetric airfoil, the airfoil may experience a local angle of attack even if the free stream is parallel to the chord line. This local effect, however, is neglected here.

In this equation the symbols r and θ in the first term are the polar coordinates measured from the fixed frame, since the body is stationary. However, the acoustic equation in the outer region is given in terms of r' and θ'. Thus, it is necessary to express r and θ in terms of r', θ', and t before any matching can take place. Although this is possible, we can demonstrate mathematically to first-order accuracy that r and θ can be replaced by r' and θ' during the process of matching. The physical explanation for this is that $\partial\gamma_m/\partial t \neq 0$ only when vortices are in the vicinity of the body, where r and θ are approximately equal to r' and θ'. Note also that by defining $z_0 = \beta\exp(i\omega_0 t)$ we implicitly assume a semblance between the fore and aft trajectory patterns; otherwise z_0 has to be defined differently.

Taking the real part and applying equation (12), we obtain

$$p_i' = \sum_{m=1}^{M} \frac{\partial \gamma_m}{\partial \tau}\frac{ds_m}{2\pi}\frac{\delta_m}{r'}\sin(\theta' - \theta_m) + \frac{\Gamma}{2\pi r'}\left[\left(\frac{Dx_1}{D\tau} + \frac{Dx_2}{D\tau}\right)\sin\theta' - \left(\frac{Dy_1}{D\tau} + \frac{Dy_2}{D\tau}\right)\cos\theta'\right] - \frac{\Gamma\omega_0}{\pi}\frac{\beta^2}{r'^2}\cos 2(\omega_0 t - \theta'). \tag{16}$$

The first term represents the fluctuation of the surface pressure, the second term is due to the interaction, and the last term represents the unsteady motion of the spinning pair. Notice that γ_m is differentiated with respect to τ since the body is fixed. Applying the Fourier transform pair

$$\hat{f}(R,\omega) = \int_{-\infty}^{\infty} f(R,t)e^{-i\omega t}dt \quad \text{and} \quad f(R,t) = \frac{1}{2\pi}\int_{-\infty}^{\infty}\hat{f}(R,\omega)e^{i\omega t}d\omega$$

to equation (16) gives the Fourier transform of p_i':

$$p_i' = \frac{M_0}{2\pi}\sum_{m=1}^{M}\frac{ds_m\delta_m}{R}\sin(\theta' - \theta_m)\int_{-\infty}^{\infty}\frac{\partial\gamma_m}{\partial t}e^{-i\omega t}dt + \frac{\Gamma M_0}{2\pi}\left[\frac{\sin\theta'}{R}\int_{-\infty}^{\infty}\left(\frac{Dx_1}{D\tau} + \frac{Dx_2}{D\tau}\right)e^{-i\omega t}dt - \frac{\cos\theta'}{R}\right.$$
$$\left.\times\int_{-\infty}^{\infty}\left(\frac{Dy_1}{D\tau} + \frac{Dy_2}{D\tau}\right)e^{-i\omega t}dt\right] - \frac{\Gamma M_0^2\omega_0\beta^2}{R^2}\left\{\cos 2\theta'\left[\delta(\omega - 2\omega_0) + \delta(\omega + 2\omega_0)\right] + i\sin 2\theta'\left[\delta(\omega + 2\omega_0) - \delta(\omega - 2\omega_0)\right]\right\}. \tag{17}$$

where $R = M_0 r'$ and $\delta(\,)$ refers to the δ-function. The second-order term is proportional to $1/R^2$, whereas the first-order term is proportional to $1/R$.

6. OUTER SOLUTIONS IN THE FREQUENCY DOMAIN

In view of the inner solution (eq. (17)), the outer solution may be assumed to have the following form:

$$p_0'(R,\theta',t) = \sum_{m=1}^{M} p_m(R,t)\sin(\theta' - \theta_m) + p_1(R,t)\sin\theta' + p_2(R,t)\cos\theta' + p_3(R,t)\sin 2\theta' + p_4(R,t)\cos 2\theta' \tag{18}$$

Substituting this expression into equation (11) gives the following equations:

$$\frac{\partial^2 q_1}{\partial R^2} + \frac{1}{R}\frac{\partial q_1}{\partial R} - \frac{1}{R^2}q_1 - \frac{\partial^2 q_1}{\partial t^2} = 0, \qquad \frac{\partial^2 q_2}{\partial R^2} + \frac{1}{R}\frac{\partial q_2}{\partial R} - \frac{4}{R^2}q_2 - \frac{\partial^2 q_2}{\partial t^2} = 0$$

where q_1 refers to p_m, p_1, or p_2, and q_2 refers to p_3 or p_4. These two equations can be transformed via the Fourier transform to two equivalent Bessel equations:

$$\frac{d^2\hat{q}_1}{dR^2}+\frac{1}{R}\frac{d\,\hat{q}_1}{dR}+\left(\omega^2-\frac{1}{R^2}\right)\hat{q}_1=0 \quad \text{and} \quad \frac{d^2\hat{q}_2}{dR^2}+\frac{1}{R}\frac{d\hat{q}_2}{dR}+\left(\omega^2-\frac{4}{R^2}\right)\hat{q}_2=0$$

whose solutions for the outgoing waves at infinity are the Hankel functions of the second kind. We, therefore, obtain

$$\hat{p}_0'=\sum_{m=1}^{M}A_m H_1^{(2)}(\omega R)\sin(\theta'-\theta_m)+A_0 H_1^{(2)}(\omega R)\sin\theta'+B_0 H_1^{(2)}(\omega R)\cos\theta'+C_0 H_2^{(2)}(\omega R)\sin 2\theta' + D_0 H_2^{(2)}(\omega R)\cos 2\theta' \quad (19)$$

where $A_m, A_0, \ldots D_0$ are the unknown coefficients to be determined by matching.

7. ASYMPTOTIC MATCHING

As mentioned briefly in Section 5, matching requires that the outer solution be put in the limiting form as $R \to 0$ (ref. 21). With the aid of the formulas given in reference 22, we have

$$\hat{p}_0' \approx \sum_{m=1}^{M}\frac{2i}{\pi\omega R}A_m\sin(\theta'-\theta_m)+\frac{2i}{\pi\omega R}(A_0\sin\theta'+B_0\cos\theta')+\frac{4i}{\pi\omega^2R^2}(C_0\sin 2\theta'+D_0\cos 2\theta')$$

Equating this equation to equation (17) gives the unknown coefficients in equation (19):

$$A_m=-\frac{iM_0\omega}{4}ds_m\delta_m\int_{-\infty}^{\infty}\frac{\partial\gamma_m}{\partial t}e^{-i\omega t}dt$$

$$A_0=-\frac{i\Gamma M_0\omega}{4}\int_{-\infty}^{\infty}\left(\frac{Dx_1}{D\tau}+\frac{Dx_2}{D\tau}\right)e^{-\omega t}dt$$

$$B_0=-\frac{i\Gamma M_0\omega}{4}\int_{-\infty}^{\infty}\left(\frac{Dy_1}{D\tau}+\frac{Dy_2}{D\tau}\right)e^{-i\omega t}dt$$

$$C_0=-\frac{\pi\Gamma M_0^2\beta^2\omega_0}{4}\omega^2\left[\delta(\omega+2\omega_0)-\delta(\omega-2\omega_0)\right]$$

$$\frac{\partial^2 p'}{\partial R^2}+\frac{1}{R}\frac{\partial p'}{\partial R}+\frac{1}{R^2}\frac{\partial^2 p'}{\partial\theta^2}-\frac{\partial^2 p'}{\partial t'^2}=0 \quad (11)$$

With the coefficients defined, we apply the Fourier inverse transform to equation (19) to give the acoustic pressure in the far field:

$$p'=-\frac{iM_0}{8\pi}\sum_{m=1}^{M}ds_m\delta_m\sin(\theta'-\theta_m)\int_{-\infty}^{\infty}\omega H_1^{(2)}(\omega R)e^{i\omega t}d\omega\int_{-\infty}^{\infty}\frac{\partial\gamma_m}{\partial\xi}e^{-i\omega\xi}d\xi-\frac{i\Gamma M_0}{8\pi}\sin\theta'\int_{-\infty}^{\infty}\omega H_1^{(2)}(\omega R)e^{i\omega t}d\omega$$
$$\times\int_{-\infty}^{\infty}\left(\frac{Dx_1}{D\xi}+\frac{Dx_2}{D\xi}\right)e^{-i\omega\xi}d\xi+\frac{i\Gamma M_0}{8\pi}\cos\theta'\int_{-\infty}^{\infty}\omega H_1^{(2)}(\omega R)e^{i\omega t}d\omega\int_{-\infty}^{\infty}\left(\frac{Dy_1}{D\xi}+\frac{Dy_2}{D\xi}\right)e^{-i\omega\xi}d\xi$$
$$+\Gamma M_0^2\omega_0^3\beta^2\left[J_2(2\omega_0R)\sin 2(\theta'+\omega_0t)-Y_2(2\omega_0R)\cos 2(\theta'+\omega_0t)\right] \quad (21)$$

The last term, written in terms of Bessel functions of the first and the second kind, $J_2(2\omega_0 R)$ and $Y_2(2\omega_0 R)$, refers to the background noise that will be heard by the observer constantly. All other terms represent the interaction sound, which will be heard by the observer in the interval when the vortices are near the body.

The remaining task is to evaluate the Fourier integrals in equation (21). Two procedures are generally available. One is to use the discrete Fourier transform, and the other is to rewrite the integrals as convolution integrals. These convolution integrals are akin to the divergent integrals of the Hadamard type and have to be evaluated accordingly. These two procedures will be discussed separately.

8. METHOD OF DISCRETE FOURIER TRANSFORM

Although the term $\omega H_1^{(2)}(\omega R)$ in the inverse integrals in equation (21) approaches $\omega^{1/2}$ as $\omega \to \infty$, the pulse functions such as $\partial\gamma_m/\partial\xi$ are basically of the triangular wave forms whose Fourier transforms decay like $1/\omega^2$ at infinity. Thus, the function as a whole is absolutely integrable, and the inverse integral exists. On this basis, the existing methods for the discrete Fourier transform, such as those stated in reference 23, can be used. In order to provide some assurance that this method was being applied properly, we repeated Crighton's solution numerically (ref. 10) and found a close agreement with his results.

9. METHOD OF CONVOLUTION INTEGRAL

The procedure of writing the Fourier integrals in equation (21) in terms of convolution integrals was developed by Conlisk and coworkers (see ref. 13 and related papers). To our knowledge, no actual evaluation of these integrals has been made. Their concern has been with the near-field sound, which does not require evaluation. A close look at their procedure suggests some questionable steps may have been taken. Such steps could be the reason that the resulting integrals become divergent and are of the Hadamard type. However, the evidence that we have, on the basis of actual evaluation, seems to indicate that these steps did not totally invalidate the outcome, except the emergence of divergent integrals. With the help of Hadamard's definition of the final part (ref. 16 or 24), the physically meaningful part of the integral is extracted and the meaningless part is discarded. Perhaps for this reason, the acoustic pressure in the far field based on convolution integrals agrees reasonably well with some existing solutions under certain circumstances. However, discrepancies begin to develop if the interaction becomes strong and vortices are very close to the surface. This anomaly may be common to the methods using discrete vortex filaments with singular centers, as was also mentioned by Hardin and Mason.

In order to make the explanation easier, let us repeat some of the steps in reference 13. Equation (21) contains many terms, but they are all similar. It is, therefore, sufficient to pick only one term for illustration:

$$-\frac{i\Gamma M_0}{8\pi}\int_{-\infty}^{\infty}\omega H_1^{(2)}(\omega R)e^{i\omega t}d\omega\int_{-\infty}^{\infty}\frac{Dx_1}{D\xi}e^{-i\omega\xi}d\xi=-\frac{i\Gamma M_0}{8\pi}\int_{-\infty}^{\infty}\frac{Dx_1}{D\xi}d\xi\int_{-\infty}^{\infty}\omega H_1^{(2)}(\omega R)e^{i\omega(t-\xi)}d\omega \tag{22}$$

The purpose of this step is to change the order of integration, which is permissible if the functions are square-integrable (see p. 27 in ref. 25). However, as mentioned previously, $\omega H_1^{(2)}(\omega R) \to \omega^{1/2}$ as $\omega \to \infty$. The square-integrability criterion $\int_{-\infty}^{\infty}\left|\omega H_1^{(2)}(\omega R)\right|^2 d\omega < \infty$ is therefore not satisfied.

Assuming this step is valid, we still have to write $H_1^{(2)}(\omega R)$ in terms of the modified Bessel function $K_1(\,)$ before we can consult a table. Equation (22) can now be reduced to

$$-\frac{i\Gamma M_0}{8\pi}\int_{-\infty}^{\infty}\omega H_1^{(2)}(\omega R)e^{i\omega t}d\omega\int_{-\infty}^{\infty}\frac{Dx_1}{D\xi}e^{-i\omega\xi}d\xi=-\frac{i\Gamma M_0}{8\pi}\left(\frac{-2}{\pi}\right)\int_{-\infty}^{\infty}\frac{Dx_1}{D\xi}d\xi\int_{-\infty}^{\infty}\omega K_1(i\omega R)e^{i\omega(t-\xi)}d\omega$$

$$=-\frac{\Gamma M_0 R}{4\pi}\int_{-\infty}^{t-R}\frac{Dx_1}{D\xi}\frac{d\xi}{\left[(t-\xi)^2-R^2\right]^{3/2}} \tag{23}$$

Although we formally obtain a convolution integral, an improper use of the table has been made. For example, reference 26 states explicitly that the parameter in $K_1(\,)$ must be real and positive. This constraint is violated in the above equation. We nevertheless consider that this method has its merit as will be demonstrated later.

The convolution integral in equation (23) is similar to the acoustic potential function given in reference 13, which has to be differentiated in order to obtain the acoustic pressure. However, special care is needed when a divergent integral is involved. For this reason p' is chosen as the dependent variable instead of the acoustic potential.

Divergent integrals similar to that in equation (23) have also been encountered in the linearized theory of supersonic flow (slender-body theory), which is known to be equivalent to the acoustic theory. Furthermore, the present convolution integral is of the Hadamard type. Therefore, existing methods (ref. 16 or 24, for example) can be used to define the final part. A brief description is given here to better illustrate a point that may affect the accuracy of some numerical results.

Using $f(\xi)$ to represent $Dx_1/D\xi$, we may write equation (23) as

$$\int_{-\infty}^{t-R} \frac{f(\xi)d\xi}{\left[(t-\xi)^2 - R^2\right]^{3/2}} = \int_{-\infty}^{t-R} \frac{f(\xi) - f(t-R)}{\left[(t-\xi)^2 - R^2\right]^{3/2}} d\xi + f(t-R) \int_{-\infty}^{t-R} \frac{d\xi}{\left[(t-\xi)^2 - R^2\right]^{3/2}}$$

The first integral on the right side of the equation can be shown to be an ordinary improper integral and may be evaluated accordingly. The second integral is a divergent integral and has to be determined by using Hadamard's definition of the final part. We now write the first integral to be a sum of two parts with σ denoting a small quantity

$$\int_{-\infty}^{t-R} \frac{f(\xi) - f(t-R)}{\left[(t-\xi)^2 - R^2\right]^{3/2}} d\xi = \int_{-\infty}^{t-R-\sigma} \frac{f(\xi) - f(t-R)}{\left[(t-\xi)^2 - R^2\right]^{3/2}} d\xi + \int_{t-R-\sigma}^{t-R} \frac{f(\xi) - f(t-R)}{\left[(t-\xi)^2 - R^2\right]^{3/2}} d\xi \tag{24}$$

The first part is a regular integral and can be evaluated by a conventional method; the second part, after expanding $f(\xi)$ about the point $t - R$ and retaining the first-order term, becomes

$$\int_{t-R-\sigma}^{t-R} \frac{f(\xi) - f(t-R)}{\left[(t-\xi)^2 - R^2\right]^{3/2}} d\xi \approx -f'(t-R) \int_{t-R-\sigma}^{t-R} \frac{(t-R-\xi)}{(t-\xi-R)^{3/2}(t-\xi+R)^{3/2}} d\xi$$

which has a closed-form solution. Our experience seems to indicate that σ in equation (24) has to be chosen in such a way that it is comparable to the size of $\Delta\xi$. If it is too small, large local spikes may develop. Even with some precaution, this anomaly is still there and can be seen in figure 10.

10. BACKGROUND NOISE

It is perhaps worthwhile at this stage to present some evidence that the method of convolution integrals is capable of yielding reasonable results, at least under some conditions. To this end a pair of spinning vortices convected in a free space is chosen as the first test case. An analytic solution to this problem is known (ref. 9) and is, in fact, the last term in equation (21). The process leading to an analytic solution involves the use of the δ-function. If we forgo this practice, we can still proceed, but in this case convolution integrals will emerge. Taking similar steps as in equations (22) to (24), we have

$$p' = -\frac{3\Gamma}{4\pi} M_0^2 R^2 \omega_0 \beta^2 \left\{ \sin 2\theta' \int_{-\infty}^{t-R} \frac{\sin 2\omega_0 \xi}{\left[(t-\xi)^2 - R^2\right]^{5/2}} d\xi + \cos 2\theta' \int_{-\infty}^{t-R} \frac{\cos 2\omega_0 \xi}{\left[(t-\xi)^2 - R^2\right]^{5/2}} d\xi \right\} \tag{25}$$

This expression is similar to equation (23), except that the denominator in the integrand is raised to 5/2 power instead of 3/2 power, which occurs because the acoustic pressure for a spinning pair is a second-order effect.

Figure 10 compares two sets of p'. Although the frequency and the amplitude given by equation (25) are both somewhat larger than the analytic quantities, the agreement is not really bad, especially in view of the fact that the solution given in equation (25) involves two divergent integrals. In the present formulation, which uses the convective acoustic equation, the Doppler effect on acoustic radiation should appear by itself. Although this property cannot be seen easily in figure 10, it will be discernible at a higher Mach number—for example, at $M_0 \geq 0.3$.

The acoustic pressure depicted in figure 10 may be assumed to represent the background noise in the problem of a vortex/body interaction, if the fore and aft trajectories are similar. If they are different, the characteristics of the background noise after interaction will be altered, that is, have a different frequency and amplitude. In this case we have to choose two sets of average values to approximate the fore pattern from $-\infty$ to x_1 and the aft pattern from x_2 to ∞. (The interval between x_1 and x_2 is the interaction zone, which is neglected as far as the background noise is concerned.) For illustration, the step modulated input $f(t) = U(t) \cos \omega_0 t$ is used to represent a cosine wave in the interval from 0 to ∞, where $U(t)$ is the unit step function. The Fourier transform of $f(t)$ is

$$\hat{f}(\omega) = \frac{\pi}{2}\left[\delta(\omega - \omega_0) + \delta(\omega + \omega_0)\right] + \frac{i\omega}{\omega_0^2 - \omega^2}$$

(See p. 41 of ref. 25.) This expression is seen to be equivalent to D_0 in equation (20). However, since it has a singular term, a special treatment is required in the inverse transform. For this reason, the method of convolution integrals is preferred.

Again following similar steps as in equations (22) to (24), we obtain

$$p' = -\frac{3\Gamma M_0^2 R^2}{4\pi} \sin 2\theta' \left\{ \omega_1 \beta_1^2 \int_{-\infty}^{t-R} \frac{U(-\xi - x_1) \sin 2\omega_1 \xi}{\left[(t-\xi)^2 - R^2\right]^{5/2}} d\xi + \omega_3 \beta_3^2 \int_{-\infty}^{t-R} \frac{U(\xi - x_2) \sin 2\omega_3 \xi}{\left[(t-\xi)^2 - R^2\right]^{5/2}} d\xi \right\} + \frac{3\Gamma M_0^2 R^2}{4\pi} \cos 2\theta'$$
$$\times \left\{ \omega_1 \beta_1^2 \int_{-\infty}^{t-R} \frac{U(-\xi - x_1) \cos 2\omega_1 \xi}{\left[(t-\xi)^2 - R^2\right]^{5/2}} d\xi + \omega_3 \beta_3^2 \int_{-\infty}^{t-R} \frac{U(\xi - x_2) \cos 2\omega_3 \xi}{\left[(t-\xi)^2 - R^2\right]^{5/2}} d\xi \right\} \quad (26)$$

where ω_1 and β_1 denote the average angular velocity and the radius of rotation in the forward portion of the trajectory, and ω_3 and β_3 denote the same for the aft portion. The symbol $-x_1$ is the endpoint of the forward portion, whereas x_2 is the starting point of the aft portion (see fig. 4(c)). The symbol $U(\,)$ refers to the unit step function shifted by the amount $-x_1$ or x_2 to account for the semi-infinite length. If the segment becomes infinitely long, the unit step function becomes unity throughout and equation (26) reduces to equation (25).

To demonstrate the applicability of equation (26), we extricated the required information from the calculated trajectories in figure 4(c) to evaluate p', which is plotted in figure 11. Notice that in this case the background noise after an interaction has been almost totally attenuated. Because of the linearity property, this noise signature can be superimposed on the acoustic radiation from an interaction to present a complete acoustic field. This is shown in the following section. However, because of the scale difference, the background noise is not discernible. For this reason, the body in figure 11 is removed and the vertical scale is enlarged.

11. RESULTS AND DISCUSSION

In the foregoing sections we discussed two methods to evaluate the Fourier integrals. The method of convolution integrals is rather complex and lacks mathematical rigor, yet it is an interesting approach and may provide simpler solutions on occasion, such as in the previous example. Furthermore, two more cases will be given to demonstrate its applicability to sound generation, provided that the interaction is moderate. For a strong interaction overpredictions are liable to occur. Thus, the discrete Fourier transform (DFT) is our primary method.

As mentioned earlier, Hardin and Mason investigated the problem of sound generation by a vortex and presented their calculated results for a Joukowski airfoil. Using the initial and boundary conditions indicated in reference 17, we simplified equation (21) for a single vortex and solved it by means of the DFT to secure a set of corresponding acoustic pressures. Figure 12 shows this comparison. The characteristic length in reference 17 is the span length. However, no such length is available in the present investigation. Consequently, only the relative magnitudes can be compared. The overall shape appears to be similar, though details are different. Although Hardin and Mason analyzed both lift and nonlifting airfoils, only the nonlifting case is compared, since the angle of attack is assumed to be zero in this study.

Observing the trajectories in figure 4, we could assume that the degree of interaction becomes progressively stronger from parts (a) to (c) of figure 4. We intend to show that as far as sound generation is concerned, this assumption is correct. For this purpose we used the DFT to solve equation (21). There is, however, a disparity in the fore and aft trajectories in parts (b) and (c) of figure 4; the last term in equation (21) for these two cases has to be replaced by equation (26). The results are plotted in figure 13, which shows that the background noise is relatively low, especially in figure 13(c). To discern the background noise in figure 13(c), refer to figure 11, which has been magnified. These three examples illustrate that the background noise is strongly affected by the dynamics of interaction, which can augment or attenuate its intensity. In the case of figure 13(c), the interaction almost silenced it.

Let us now digress to test the accuracy of the method of convolution integrals by repeating the calculation for the case in figure 13(a). The results are shown in figure 14(a). The characteristics of the curves in these two figures are approximately the same, although the intensities are dissimilar to various degrees. We take a more lenient view of this method and consider this kind of accordance to be satisfactory.

Returning to the method of DFT, let us consider the case in figure 5. The initial and boundary conditions for this case are identical to those in figure 13(c), except that $\Gamma_1 = \Gamma_2 = -0.15$. Simply changing the sign of the vortices greatly diminishes the pressure fluctuation in figure 14(b), and the first peak is now positive instead of negative. As mentioned earlier, this outcome is borne out by Howe's result. In other words, sound generation by vortex/body interaction depends on the sense of rotation. The effect is antisymmetric with respect to the chord line. For example, if the vortex in figure 5 is shifted to a corresponding position below the chord line, the trajectory will be the same as in figure 4(c), and the sound radiation will be identical to that in figure 13(c).

A possible application of this property is that if a design change is feasible, we can position the vortices on the favorable side of the body to substantially reduce the noise level. Even for a single vortex, the direction of rotation can make some difference. For example, the predictions by Hardin and Mason in figure 5 of reference 17 show the different levels of sound radiation for $\bar{Y}_o / \bar{c} = -0.2$ and +0.2, even at zero angle of attack.

A pair of fast-spinning vortices would be expected to produce a higher level of sound radiation than would a pair of slow-spinning vortices. In order to substantiate this assumption, the initial positions of the vortices in figure 4(b) was modified slightly by reducing the radius of rotation, thereby making them spin faster, as depicted in figure 6(a). The corresponding acoustic radiation calculated by the DFT is plotted in figure 15(a); it is considerably higher than that in figure 13(b).

Until now, the point of observation was assumed to be situated at $\theta = 75°$ from the positive x-axis (the chord line behind the airfoil). It would be interesting to know the sound radiation received by an observer at the same distance from the center but who is located ahead of the airfoil and slightly above the chord line ($\theta = 170°$). In this case, as displayed in figure 15(b), the intensity is reduced in comparison to figure 13(c), the signals are bunched together, and there is a time delay in receiving the signal. Such characteristics are what we would expect.

Let us now direct our attention to bluff bodies. Contrary to our intuition, it seems that sound radiation from vortex/bluff-body interactions is almost always lower than that from the vortex/airfoil interaction. The explanation lies perhaps in the flow pattern in the nose region of a bluff body, where the fluid, after impacting a flat surface, branches off into two streams and skirts the corners to be away from the body. As a result, the vortex never gets a chance to be very close to the surface, and there is less interaction. This seems to be true even for the almost head-on collision shown in figure 7(a). By contrast, a pair of spinning vortices can come very near the airfoil and practically "scrub" the surface, thereby giving rise to a strong interaction. However, it is uncertain whether the discrete vortex method is still valid, as vortices move into the boundary layer and the viscous effect becomes important. Further investigations may be needed. With an airfoil, the trailing edge may also intensify the interaction.

In order to clarify some of these intuitive explanations, in figure 16(a) we plotted acoustic pressure fluctuations for the trajectory depicted in figure 7(a). As can be seen, this pattern changed enormously after interaction. In the case for the airfoil, such a pattern would usually indicate high intensity radiation. Yet the acoustic pressure in figure 16(a) is only moderate. (Note here that the background noise is not plotted in this figure and will not be plotted hereafter since its absence will not hinder our future discussion.)

As a further test of the method of convolution integral, another example is provided. This method was used to recalculate the acoustic pressure in figure 16(a). The results (see fig. 16(b)) show that the details are again at variance with figure 16(a), but the intensity is comparable.

As in figure 13, we can increase the intensity of the acoustic pressure by manipulating the vortex pair's horizontal distance from the leading edge. With a proper shift, the acoustic pressure can be increased considerably (see fig. 17(a)), but it is still significantly less than that in figure 13(c). To lower the intensity further, simply round off the corners slightly as in figure 3(b) or figure 8(b), and the pressure fluctuation (fig. 17(b)) lessens substantially. By shifting the vortex pair somewhat upward and away from the centerline, the serrate peaks in figure 17 give way to the smooth curve in figure 18. This transition from a serrate configuration to a smooth curve also occurs in a vortex/airfoil interaction.

Finally, let us investigate the cases of three and four spinning vortices. In order to explain the scaling effect of interaction, it is more convenient to pick the system of four vortices (fig. 6(c)). As in the previous cases, these are equal and like-signed vortices that are spaced uniformly around a circle (fig. 1) and spin at a constant rate in a stationary medium (eq. (8)). Now we can remove two trailing vortices to form a pair of stacked vortices, as in previous dispositions, thereby making the rotation radius smaller. The acoustic radiation from the interaction of this pair with the airfoil is plotted as a solid line in figure 19(b). Next, the two previously removed vortices are restored to form a quadruple. This system, however, spins at a rate 1.5 times faster than the rate of the pair, so the acoustic pressure becomes substantially higher as shown in figure 19(b). (The motion of four vortices in the present configuration is known to be stable (ref. 19), and there is no computational evidence of instability after interaction.)

It is proposed that the increase in acoustic pressure with the quadruple (fig. 19(b)) is almost entirely due to the increase in rotational speed and nearly independent of the number of vortices involved. To illustrate this scaling factor, let us reduce the vortex strength for the quadruple from 0.15 to 0.1, so that the rate of spinning matches that of the pair, and recompute the acoustic pressure. This is represented by the dashed line in figure 19(a), which differs only moderately from the solid line. This scaling effect should also be valid for a system of three vortices and for bodies other than an airfoil; both of these cases are demonstrated next.

Knowing the trajectory pattern in figure 6(b) and following a procedure similar to that just discussed, we plotted the solid lines in figure 20(a) to represent the acoustic pressure after the third trailing vortex is removed (fig. 1). Restoring this vortex to the system produces radiation that is much more intense (see fig. 20(b)). If we then reduce the vortex strength in a similar manner to make the two rotating speeds identical, we obtain the dashed lines shown in figure 20(a). These two sets of lines agree fairly well, so the scaling factor is again validated.

It is pertinent to make another remark here. The scaling factor is expected to hold true for bluff bodies under most circumstances; however, it may not be valid for strong vortex/airfoil interactions because one or more vortices may scrub the surface. If the number of vortices is reduced, the likelihood of a close encounter is different.

Although some indirect comparisons have been made herein, there is a genuine need for detailed comparisons with experimental data. The challenge to developing an experiment that simulates a two-dimensional flow may be alleviated if three-dimensional problems can be solved. This is feasible, especially if the body is relatively simple and the self-induced velocity on the curved vortex filament is calculated approximately. See, for example, reference 27.

12. CONCLUDING REMARKS

A procedure to solve aeroacoustics problems due to vortex/body interactions in low-speed flow has been presented. An attempt was first made to understand the dynamics of a vortex/body interaction. It so happened that this is a rather complex process that led to some interesting properties, which were discussed in some detail. In this report only cases of zero angle of attack were investigated. However, extension to cases of nonzero angles of attack is relatively straightforward.

The method of asymptotic matching enabled us to separate the problem into two parts: an inner potential flow region and an outer acoustics region. The main advantage of this is the efficacy of dealing with a complex geometry because only the potential flow sees the geometry, and there are efficient numerical methods for solving flow problems of an arbitrary body. Matching was applied merely to transmit the gross properties of the inner region to the acoustic field. In fact the solution of acoustic pressure in the frequency domain is known; only the unknown coefficients had to be determined by matching.

A fair amount of effort has been devoted to delineating the problems associated with the method of convolution integral and to demonstrate the usage of Hadamard's definition of the final part. The evaluation of the convolution integral is not essential to solving acoustics problems, but it is of some interest in unraveling the vexing properties of a divergent integral.

The evidence from examining calculated sound generation seems to indicate that sound radiation from a vortex/bluff-body interaction is actually less than that from a corresponding vortex/airfoil interaction. Although this may appear to be paradoxical, there is an explanation for this property. We found a scaling factor that governs the sound generated by the vortex interaction and a mechanism to attenuate the background noise. In addition, we proposed a possible application that can lower sound production by simply positioning vortices on the "correct" side of the body instead of the "wrong" side.

REFERENCES

1. Powell, A.: Theory of Vortex Sound. Acoust. Soc. Am. J., vol. 36, Jan. 1964, pp. 177–195.
2. Blake, W.K.: Mechanics of Flow-Induced Sound and Vibration. Academic Press, Orlando, FL, 1986.
3. Saffman, P.G.: Vortex Dynamics, Cambridge University Press, Cambridge, England, 1992.
4. Leonard, A.: Vortex Methods for Flow Simulation. J. Comp. Phy., vol. 37, Oct. 1980, pp. 289–335.
5. Tam, C.K.W.: Computational Aeroacoustics: Issues and Methods. AIAA J., vol. 33, no. 10, Oct. 1995, pp. 1788–1796.
6. Dowling, A.P.; and Ffowcs Williams, J.E.: Sound and Sources of Sound, Ellis Horwood, Chichester, England, 1983.
7. Lewis, R.I.: Surface Vorticity Modeling of Separated Flows From Two-Dimensional Bluff Bodies of Arbitrary Shape. J. Mech. Eng. Sci., vol. 23, Feb. 1981, pp. 1–12.
8. Gostelow, J.P.: Cascade Aerodynamics. Pergamon Press, Oxford, England, 1984.
9. Mueller, E.A.; and Obermeier, F.: The Spinning Vortices as a Source of Sound. Fluid Dynamics of Rotor and Fan Supported Aircraft at Subsonic Speeds, AGARD CP–22, 1967, pp. 1–8.
10. Crighton, D.G.: Radiation From Vortex Filament Method Near a Half Plane. J. Fluid Mech., vol. 51, Jan. 1972, pp. 357–362.
11. Davis, S.S.: Theory of Discrete Vortex Noise. AIAA J., vol. 13, no. 3, Mar. 1975, pp. 375–380.
12. Hardin, J.C.: Noise Radiation From the Side Edges of Flaps. AIAA J., vol. 18, 1980, pp. 549–552.
13. Conlisk, A.T.; and Veley, D.: The Generation of Noise in Impinging Vortex Motion Past a Step. Phy. Fluids, vol. 28, Oct. 1985, pp. 3004–3012.
14. Sen R.: Vortex-Oscillation Model of Airfoil Side-Edge Noise. AIAA J., vol. 35, no. 3, Mar. 1997, pp. 441–449.
15. Hu, F.Q.; Martin, J.E.; and Hussaini, M.Y.: On Computing Sound Radiation of Temporally Evolving Mixing Layer by Vortex Method and Matched Asymptotic Expansions. AIAA Paper 96–0875, 1996.
16. Hadamard, J.S.: Lectures on Cauchy's Problem in Linear Partial Differential Equations. Yale University Press, New York, NY, 1923.
17. Hardin, J.C.; and Mason, J.P.: A New Look at Sound Generation by Blade/Vortex Interaction. J. Vib., Acoust., Stress and Reliab. In Design, vol. 107, Apr. 1985, pp. 224–228.
18. Panaras, A.G.: Numerical Modeling of the Vortex/Airfoil Interaction. AIAA J., vol. 25, Jan. 1987, pp. 5–11.
19. Acheson, D.J.: Elementary Fluid Dynamics. Oxford University Press, New York, NY, 1990.
20. Goldstein, M.E.: Aeroacoustics, McGraw-Hill, New York, NY, 1976.
21. Van Dyke, M.D.: Perturbation Methods in Fluid Mechanics. The Parabolic Press, Stanford, CA, 1975.
22. Abramowitz, M.; and Stegun, I.A.: Handbook of Mathematical Functions With Formulas, Graphs, and Mathematical Tables. Dover Publications, New York, NY, 1965.
23. Brigham, E O.: The Fast Fourier Transform. Prentice-Hall, Englewood Cliffs, NJ, 1974.
24. Ward, G.N.: Linearized Theory of Steady High-Speed Flow, Cambridge University Press, Cambridge, England, 1955.
25. Papoulis, A.: The Fourier Integral and Its Applications. McGraw-Hill, New York, NY, 1962.
26. Ryzhik, I.M.; and Gradstein, I.S.: Tables of Series, Products, and Integrals. VEB Deutscher Verlag der Wissenschaften, Berlin, 1963.
27. Affes, H.; and Conlisk, A.T.: Model for Rotor Tip Vortex-Airframe Interaction. AIAA J., vol. 31, no. 12, Dec. 1993, pp. 2263–2273.

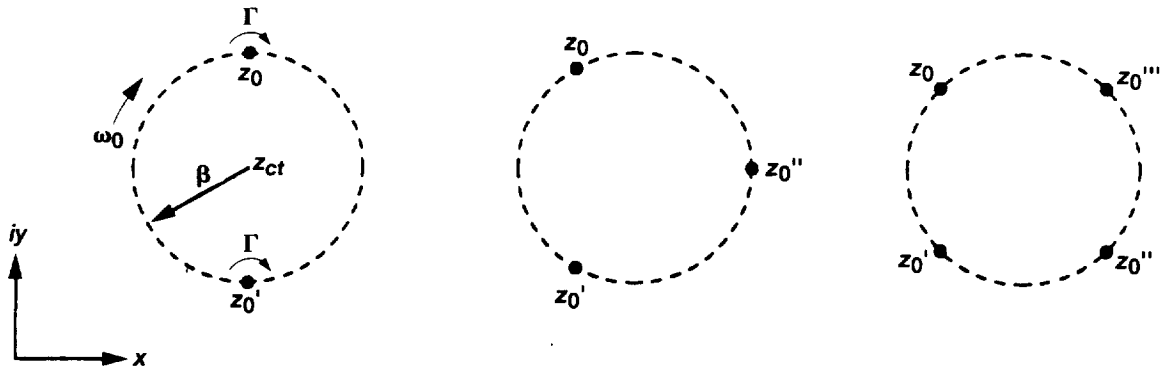

Figure 1.—Initial configurations of two, three, and four spinning vortices.

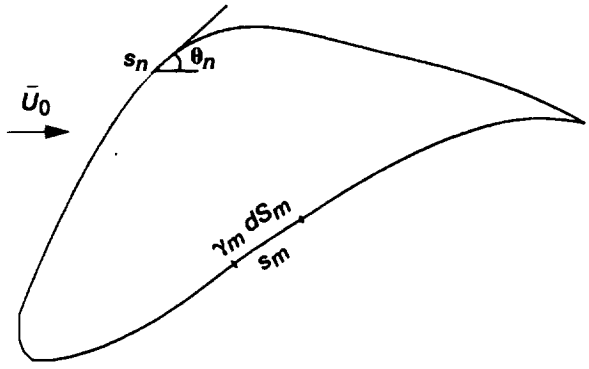

Figure 2.—Surface vorticity elements on a two-dimensional body.

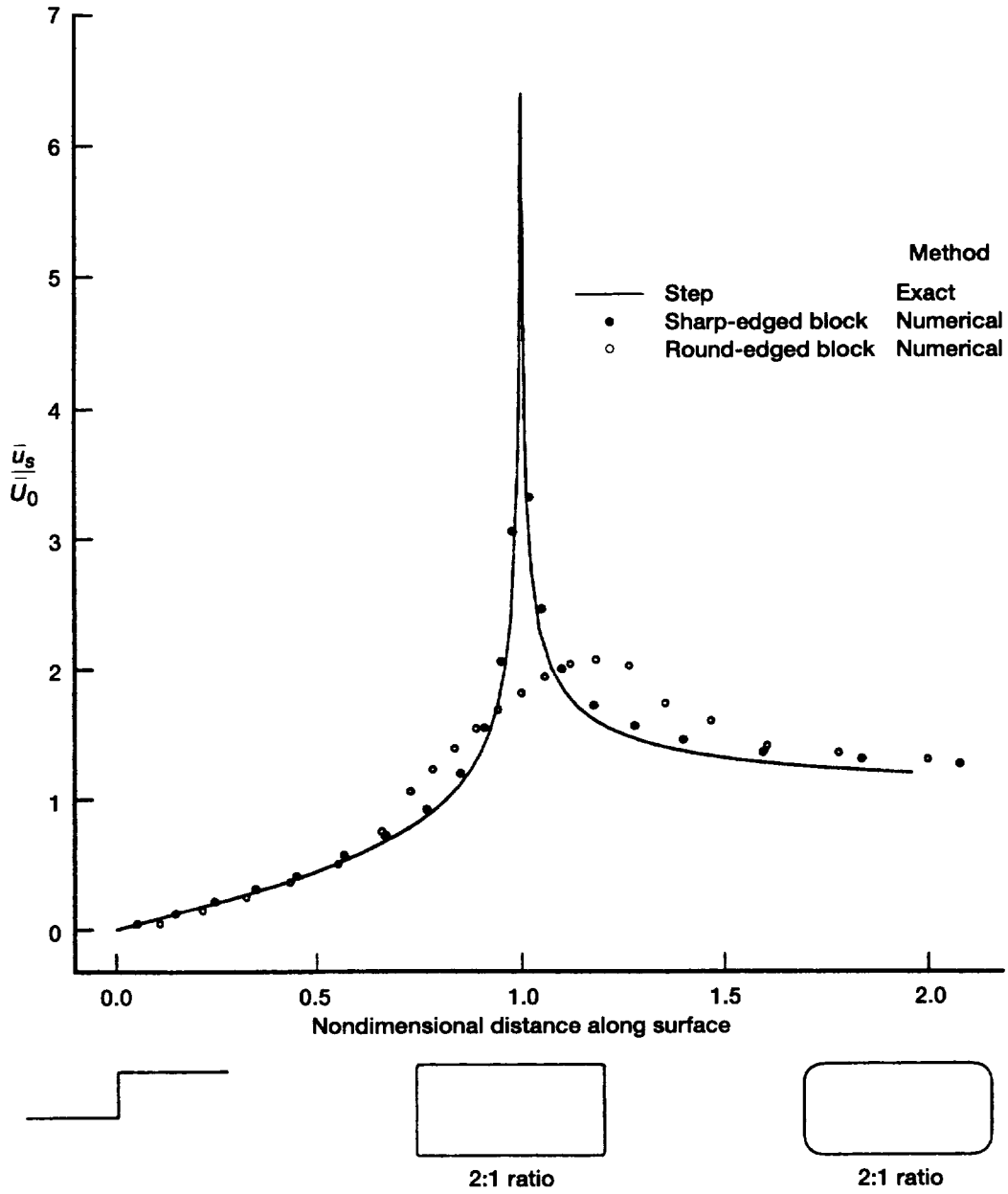

Figure 3.—Comparison of surface velocity distributions of a potential flow over a step and over two rectangular bluff bodies.

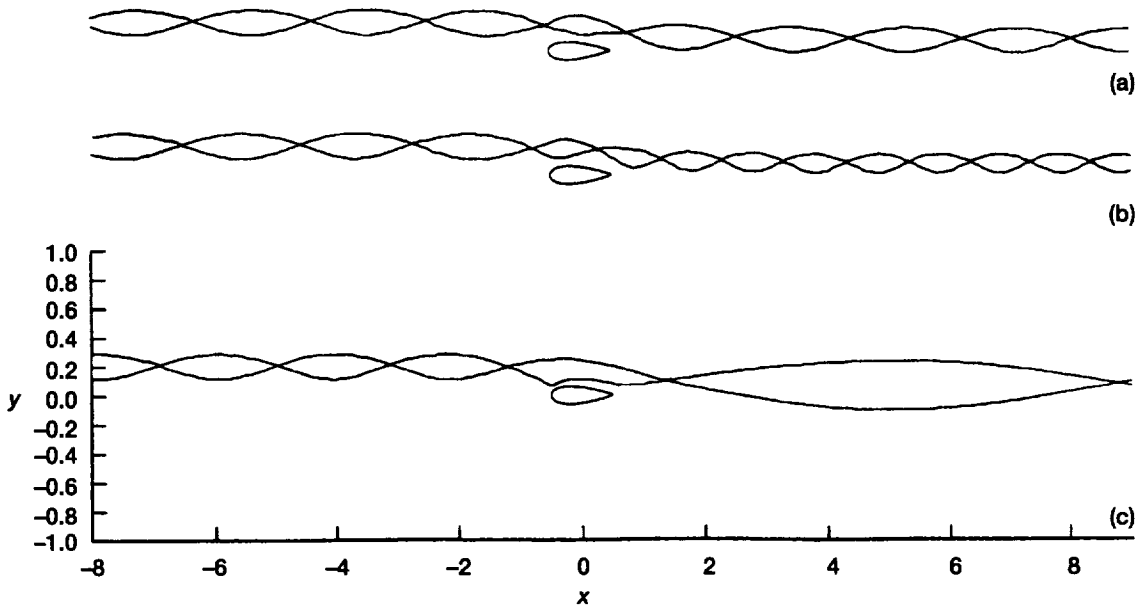

Figure 4.—Trajectories of two spinning vortices passing an NACA 0012 airfoil at zero angle of attack. For all cases, $\Gamma = 0.15$. Initial positions of vortices: (a) $z_0 = -24.4 + iy_0$ and $z'_0 = -24.4 + iy'_0$; (b) $z_0 = -24.6 + iy_0$ and $z'_0 = -24.6 + iy'_0$; and (c) $z_0 = -25.0 + iy_0$ and $z'_0 = -25.0 + iy'_0$, where $y_0 = 0.29$ and $y'_0 = 0.12$.

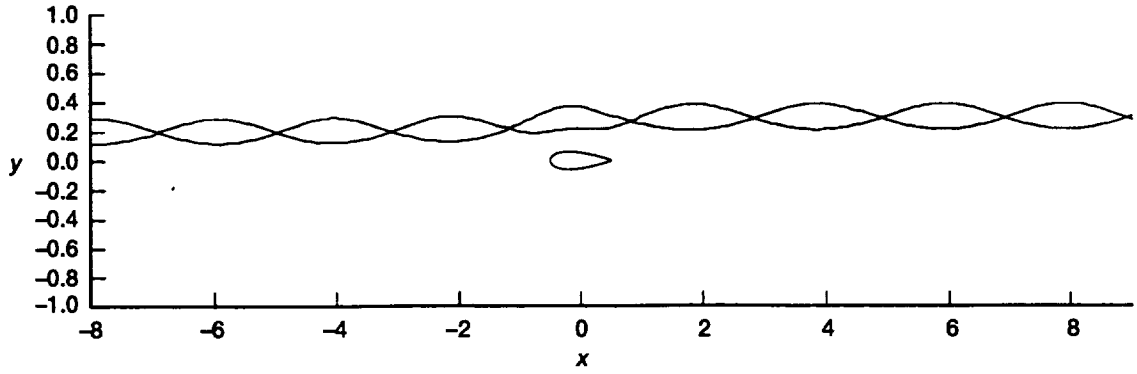

Figure 5.—Trajectories of two spinning vortices passing an NACA 0012 airfoil at zero angle of attack. Initial positions are the same as in figure 4(c): $z_0 = -25.0 + 0.29i$ and $z'_0 = -25.0 + 0.12i$, except $\Gamma = -0.15$.

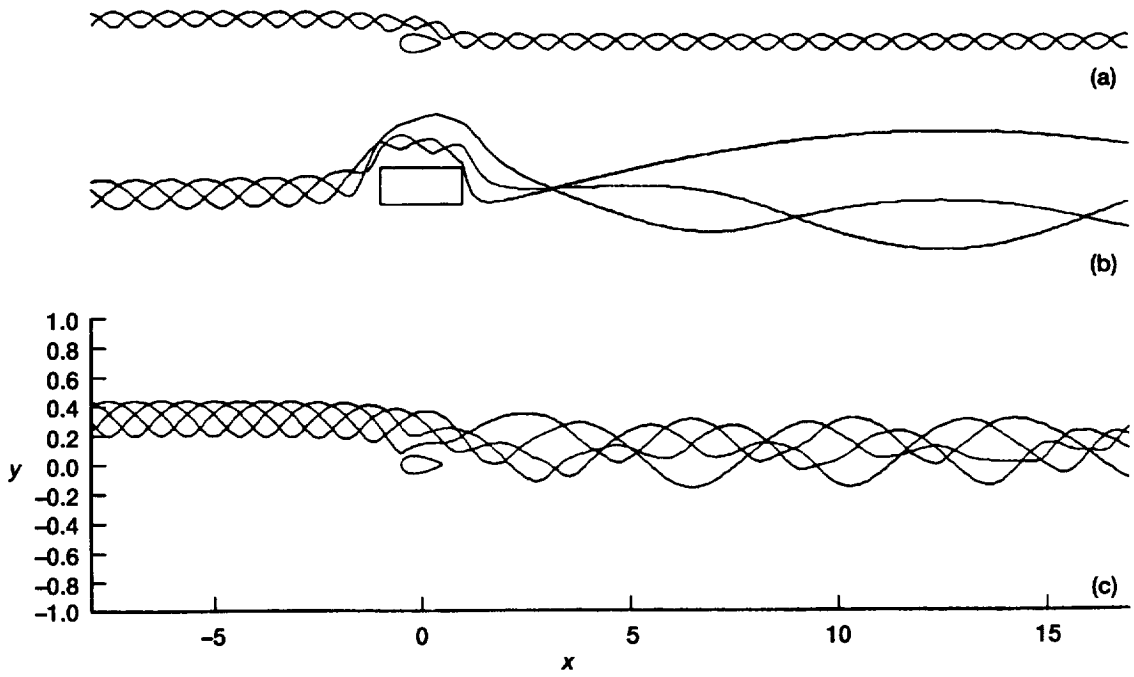

Figure 6.—Trajectories of spinning vortices at zero angle of attack. For all cases, $\Gamma = 0.15$. (a) Two vortices passing an NACA 0012 airfoil. Initial positions: $z_0 = -24.65 + 22i$ and $z'_0 = -24.65 + 0.12i$. (b) Three vortices passing a sharp-edged block. Initial positions: $z_0 = -25.7 + 0.41i$; $z'_0 = -25.7 + 0.24i$, and $z''_0 = -25.5528 + 0.325i$. (c) Four spinning vortices passing an NACA 0012 airfoil. Initial positions: $z_0 = -25.72 + 0.41i$; $z'_0 = -25.72 + 0.24i$; $z''_0 = -25.55 + 0.24i$; and $z'''_0 = -25.55 + 0.41i$.

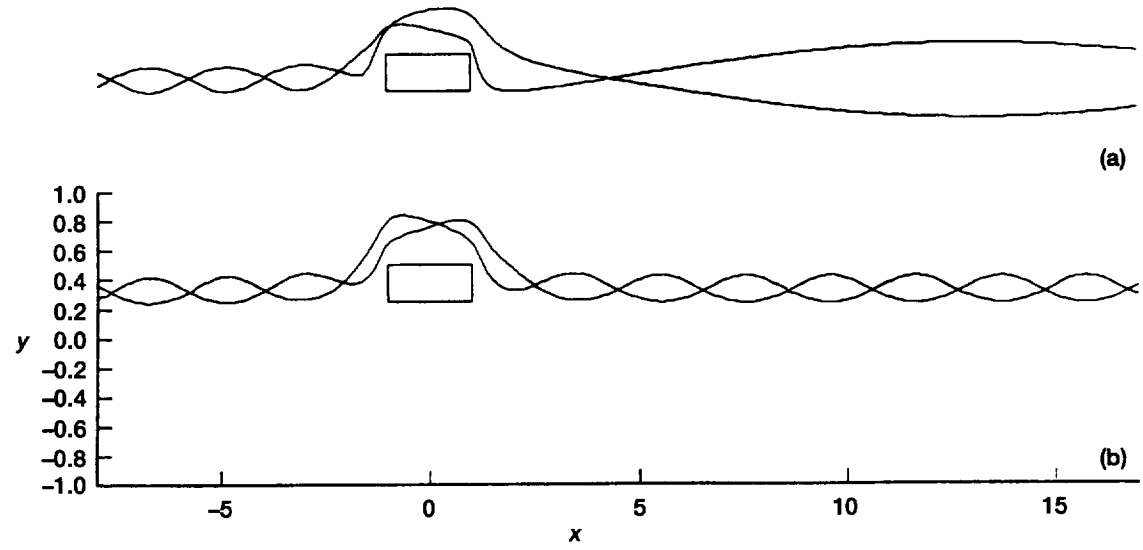

Figure 7.—Trajectories of two spinning vortices passing a sharp-edged block at zero angle of attack. Initial positions of vortices are the same for both cases: $z_0 = -25.7 + 0.41i$ and $z'_0 = -25.7 + 0.24i$. (a) $\Gamma = 0.15$. (b) $\Gamma = -0.15$.

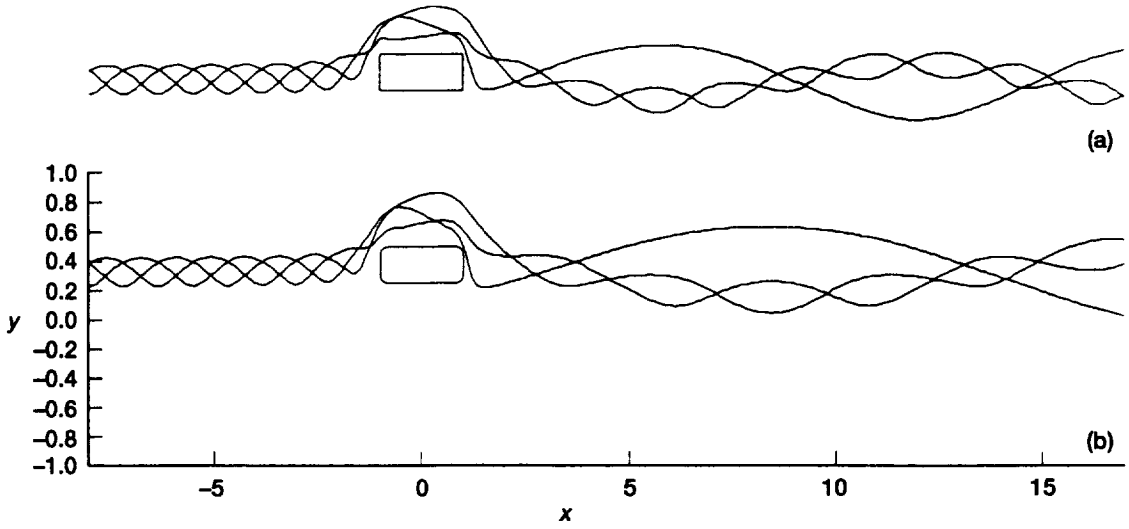

Figure 8.—Trajectories of three spinning vortices at zero angle of attack. Initial conditions are identical for both cases: $\Gamma = 0.15$; $z_0 = -25.55 + 0.41i$; $z'_0 = -25.55 + 0.24i$; and $z''_0 = -25.4028 + 0.325i$. (a) Sharp-edged block. (b) Equivalent round-edged block.

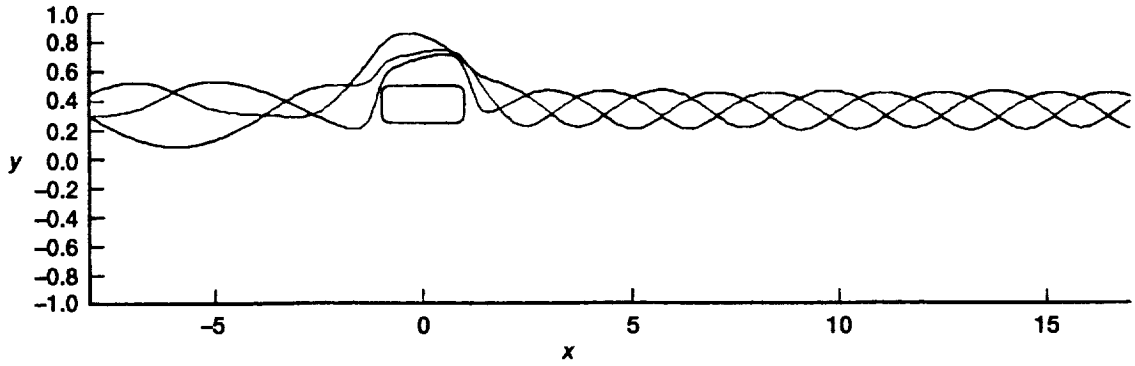

Figure 9.—Vortex trajectories rectified by a round-edged bluff body at zero angle of attack. Initial conditions: $\Gamma = 0.15$; $z_0 = -25.55 + 0.41i$; $z'_0 = -25.55 + 0.24i$; and $z''_0 = -25.19 + 0.325i$.

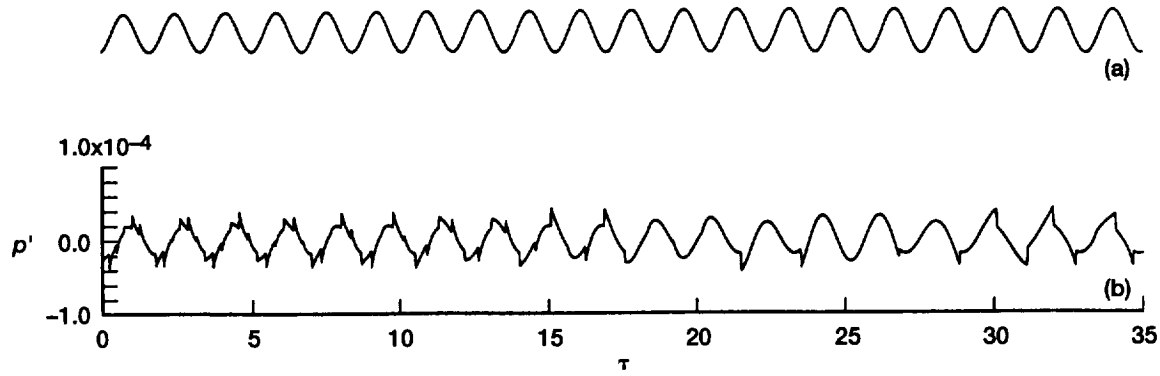

Figure 10.—Comparison of sound generation by two convected spinning vortices. (M_0 = 0.2; dt = 0.025; point of observation: R = 9.0, θ = 75° from positive x-axis.) (a) Analytic solution. (b) Method of convolution integral.

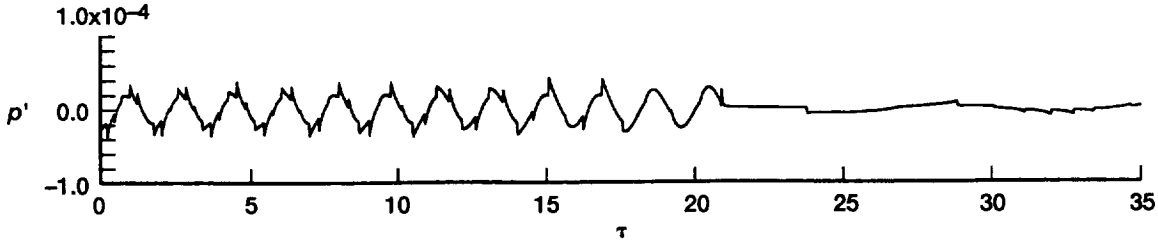

Figure 11.—Background noise due to a pair of spinning vortices attenuated by an NACA 0012 airfoil (same as the background noise in fig. 13(c) but plotted on enlarged scale).

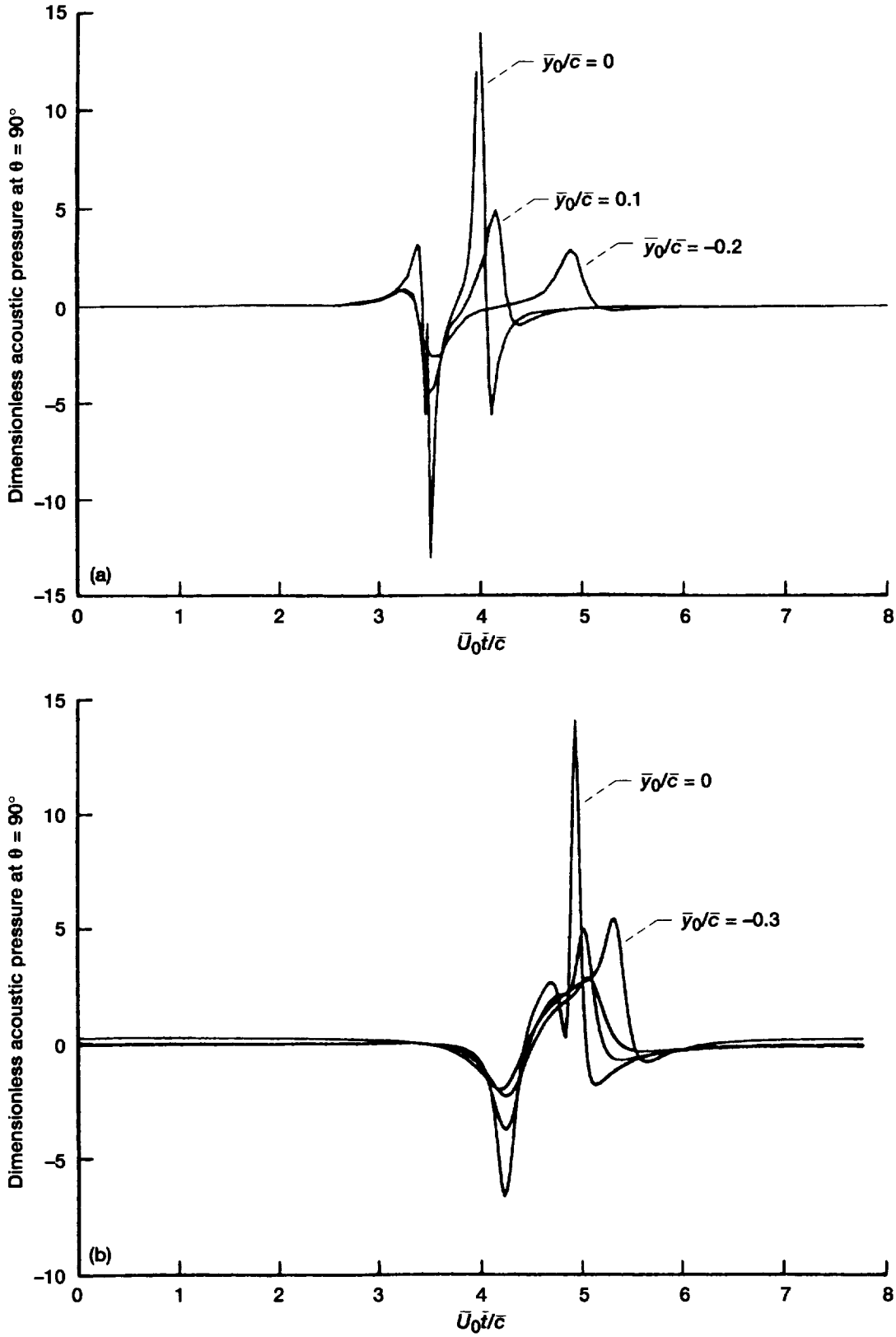

Figure 12.—Comparison of two methods for determining sound generation by a vortex interacting with Joukowski airfoil at zero angle of attack. Observer is directly above airfoil (θ = 90°). (a) Hardin and Mason's results. (b) Results from discrete Fourier transform.

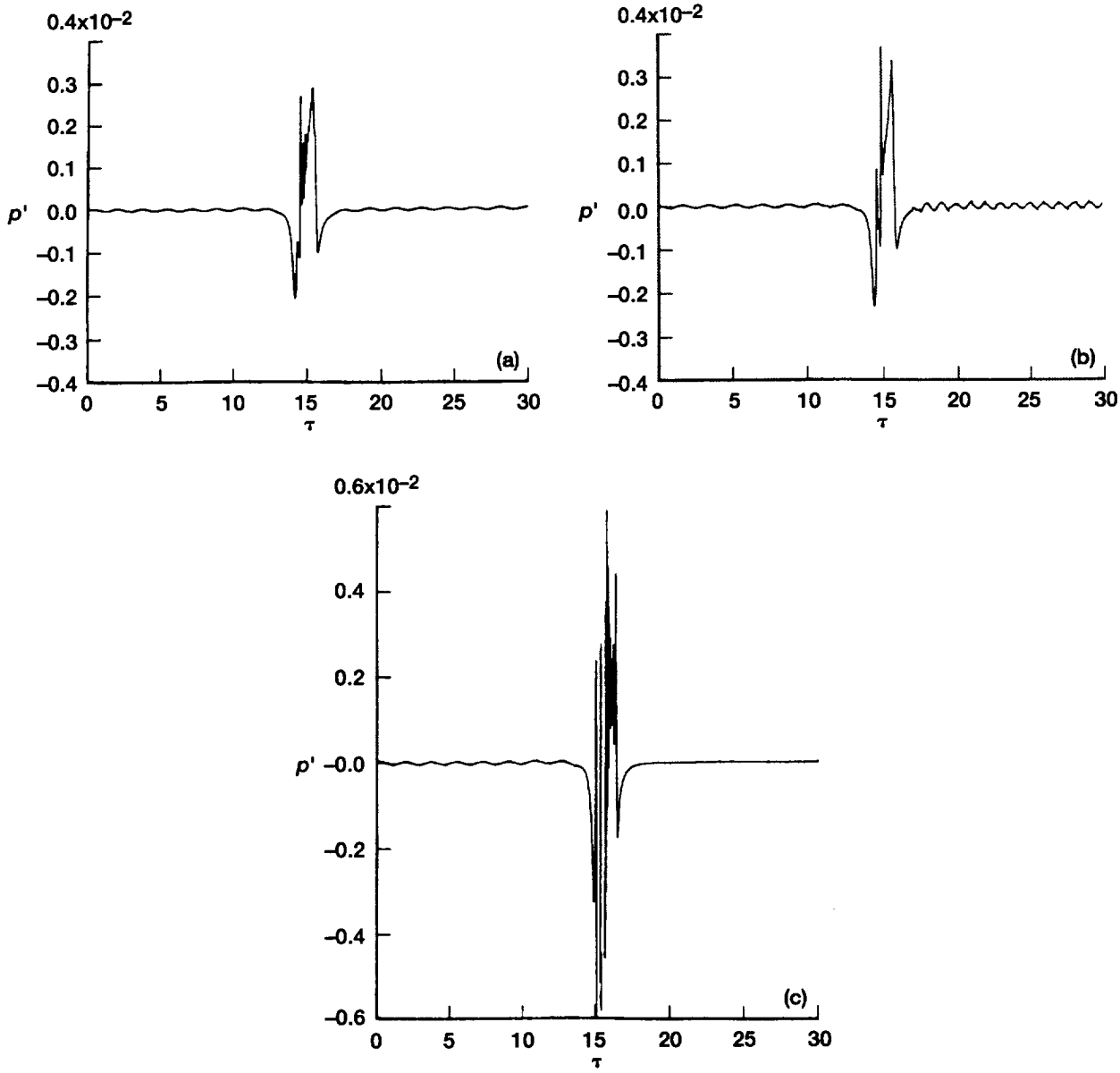

Figure 13.—Sound generation by a pair of spinning vortices interacting with an NACA 0012 airfoil. (For all cases, $\Gamma = 0.15$, $M_0 = 0.2$, $dt = 0.0125$, and point of observation is $R = 9.0$, $\theta = 75°$ from positive x-axis.) Initial positions of vortices are the same as in figures 4(a) to (c): (a) $z_0 = -24.4 + iy_0$ and $z'_0 = -24.4 + iy'_0$; (b) $z_0 = -24.6 + iy_0$ and $z'_0 = -24.6 + iy'_0$; and (c) $z_0 = -25.0 + iy_0$ and $z'_0 = -25.0 + iy'_0$, where $y_0 = 0.29$ and $y'_0 = 0.12$.

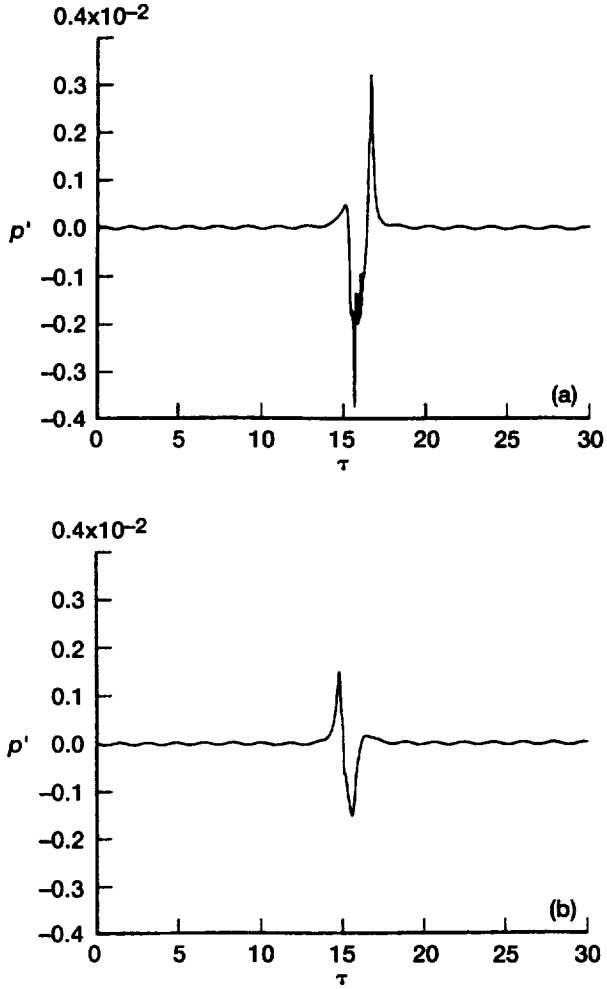

Figure 14.— Sound generation by a pair of spinning vortices interacting with an NACA 0012 airfoil. (For both cases $M_0 = 0.2$; point of observation: $R = 9.0$, $\theta = 75°$ from positive x-axis.) Initial positions are the same as in figure 4(c): $z_0 = -25.0 + 0.29i$ and $z'_0 = -25.0 + 0.12i$. (a) Convolution integral, $\Gamma = 0.15$, $dt = 0.025$. (b) Discrete Fourier transform, $\Gamma = -0.15$, $dt = 0.0125$.

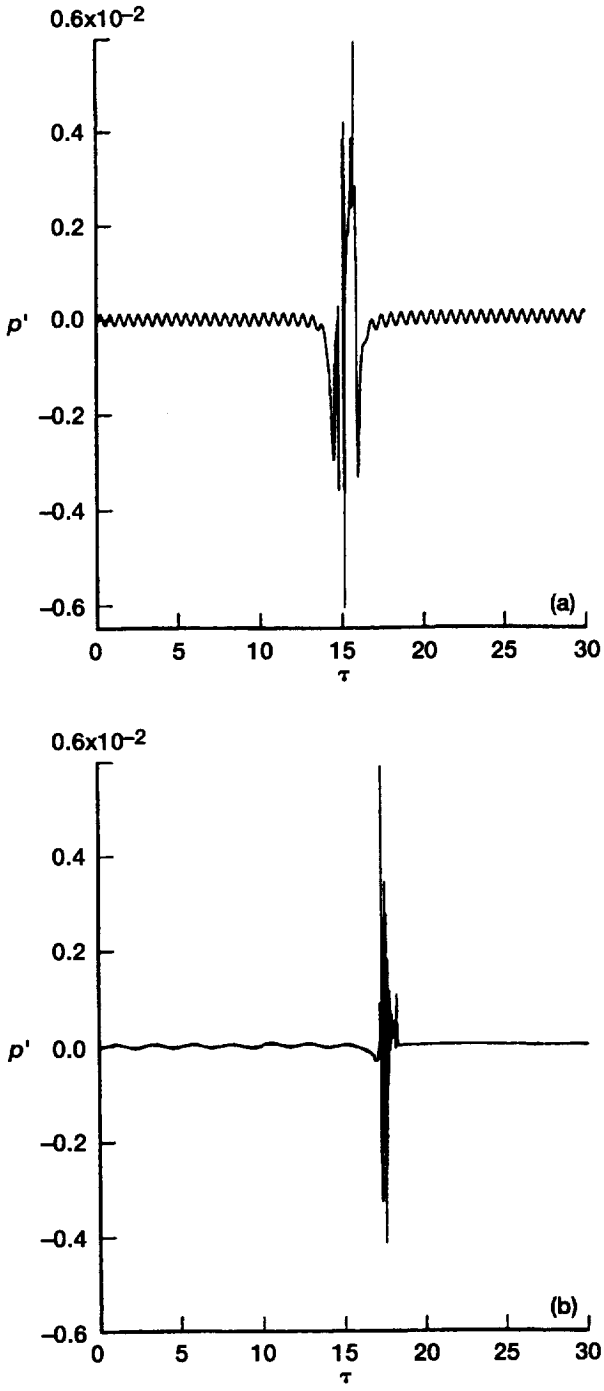

Figure 15.—Sound generation by a pair of spinning vortices interacting with an NACA 0012 airfoil. (For both cases $M_0 = 0.2$; $dt = 0.0125$; point of observation: $R = 9.0$.) (a) Faster spinning vortices with initial positions the same as in figure 6(a): $z_0 = -24.65 + 22i$ and $z'_0 = -24.65 + 0.12i$, $\theta = 75°$ from positive x-axis. (b) Recalculation of sound generation for the same initial positions, except $\theta = 170°$.

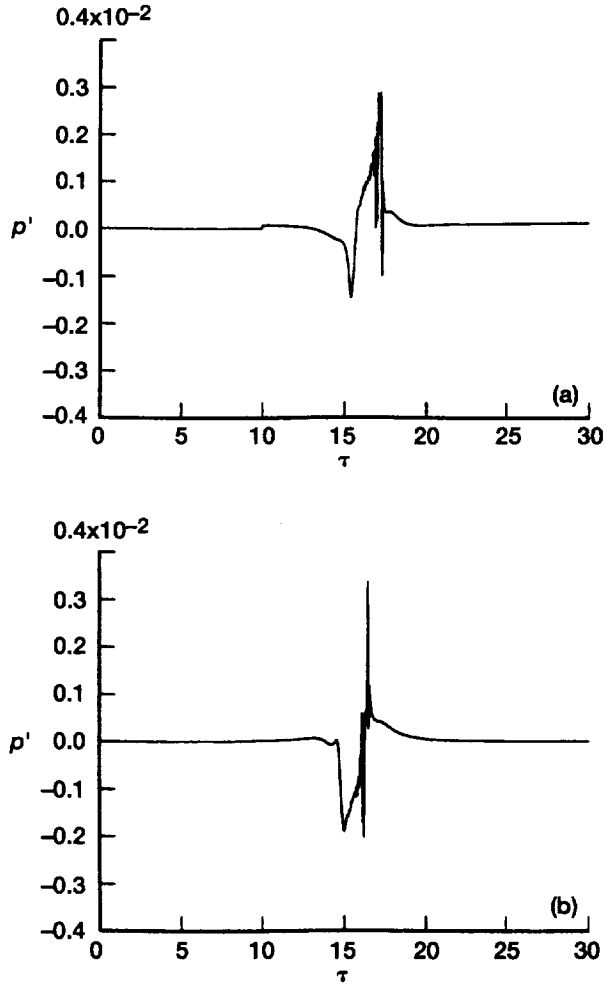

Figure 16.—Sound generation corresponding to trajectories in figure 7(a) for a pair of spinning vortices. (For both cases $M_0 = 0.2$; point of observation: $R = 9.0$, $\theta = 75°$ from positive x-axis.) (a) Discrete Fourier transform, $dt = 0.0125$. (b) Convolution integral, $dt = 0.025$.

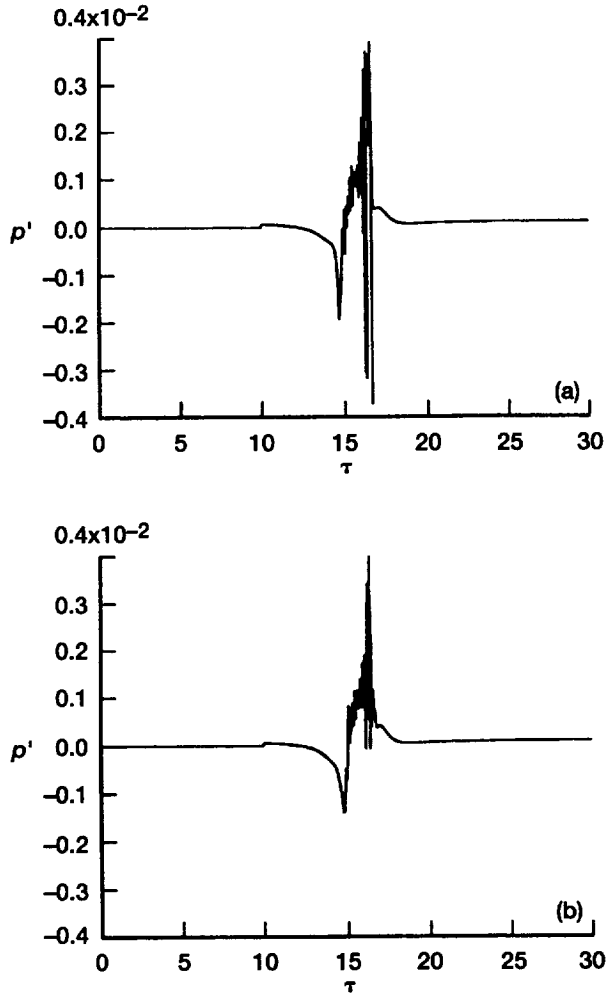

Figure 17.—Sound radiation by two spinning vortices interacting with rectangular blocks. Initial positions: $\Gamma = 0.15$, $z_0 = -25.0 + 0.41i$ and $z'_0 = -25.0 + 0.24i$. (For both cases $M_0 = 0.2$; $dt = 0.0125$; point of observation: $R = 9.0$, $\theta = 75°$ from positive x-axis.) (a) Sharp-edged block. (b) Equivalent round-edged block.

Figure 18.—Sound generation by two spinning vortices skirting a sharp-edged block. Initial positions: $\Gamma = 0.15$, $z_0 = -25.0 + 0.52i$ and $z'_0 = -25.0 + 0.35i$. ($M_0 = 0.2$; $dt = 0.0125$; point of observation: $R = 9.0$, $\theta = 75°$ from positive x-axis.)

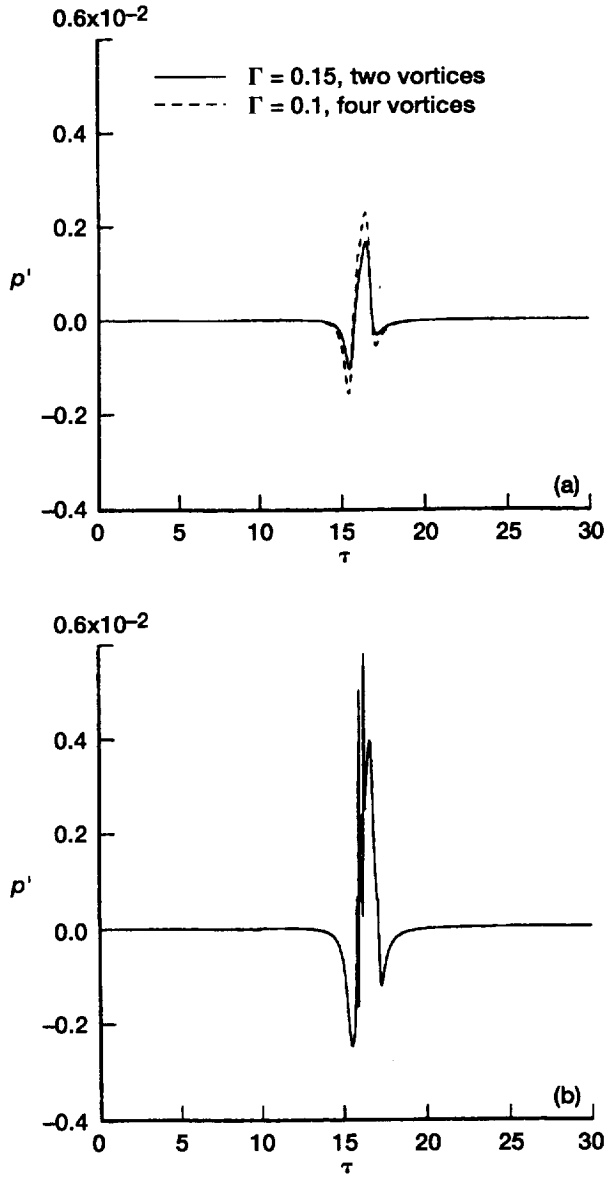

Figure 19.—Scaling factor for acoustic radiation from two and four spinning vortices interacting with an NACA 0012 airfoil. (For both cases $M_0 = 0.2$; $dt = 0.0125$; point of observation: $R = 9.0$, $\theta = 75°$ from positive x-axis.) (a) Two vortices and four vortices. (b) Four vortices corresponding to the initial positions in figure 6(c): $\Gamma = 0.15$, $z_0 = -25.72 + 0.41i$; $z'_0 = -25.72 + 0.24i$; $z''_0 = -25.55 + 0.24i$; and $z'''_0 = -25.55 + 0.41i$.

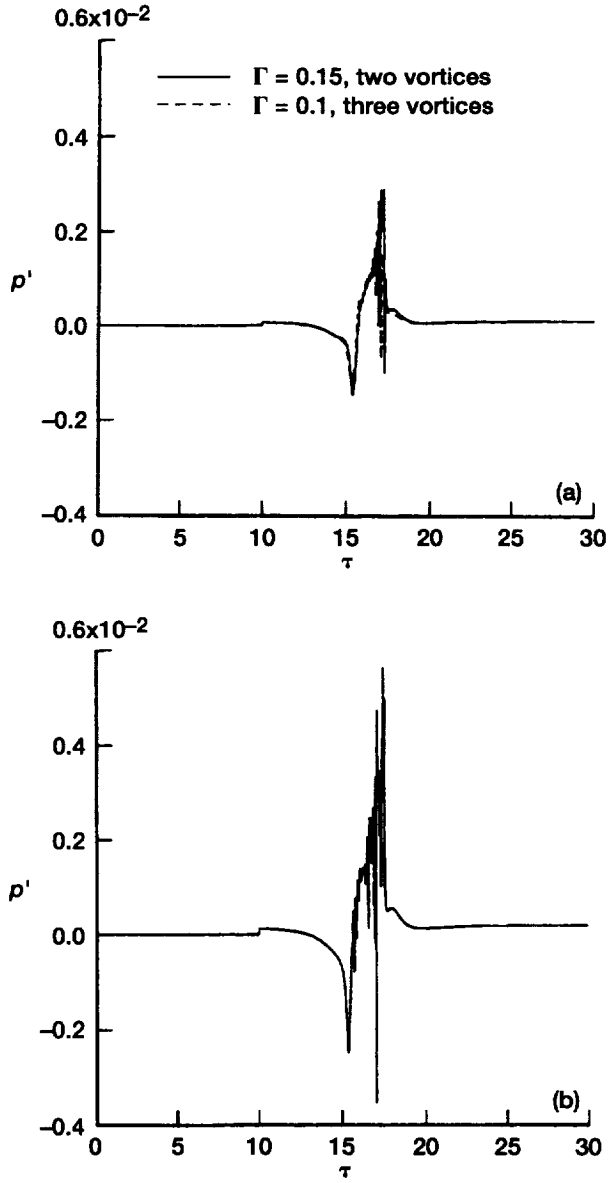

Figure 20.— Scaling factor for acoustic radiation from two and three spinning vortices interacting with a sharp-edged block. (For both cases $M_0 = 0.2$; $dt = 0.0125$; point of observation: $R = 9.0$, $\theta = 75°$ from positive x-axis.) (a) Two vortices and three vortices. (b) Three vortices corresponding to the initial positions in figure 6(b): $\Gamma = 0.15$, $z_0 = -25.7 + 0.41i$; $z'_0 = -25.7 + 0.24i$, and $z''_0 = -25.5528 + 0.325i$.

REPORT DOCUMENTATION PAGE

Form Approved
OMB No. 0704-0188

1. AGENCY USE ONLY (*Leave blank*)	2. REPORT DATE	3. REPORT TYPE AND DATES COVERED
	September 1998	Technical Memorandum

4. TITLE AND SUBTITLE

Vortex/Body Interaction and Sound Generation in Low-Speed Flow

5. FUNDING NUMBERS

WU-522-31-23-00

6. AUTHOR(S)

Hsiao C. Kao

7. PERFORMING ORGANIZATION NAME(S) AND ADDRESS(ES)

National Aeronautics and Space Administration
Lewis Research Center
Cleveland, Ohio 44135-3191

8. PERFORMING ORGANIZATION REPORT NUMBER

E-11235

9. SPONSORING/MONITORING AGENCY NAME(S) AND ADDRESS(ES)

National Aeronautics and Space Administration
Washington, DC 20546-0001

10. SPONSORING/MONITORING AGENCY REPORT NUMBER

NASA TM—1998-208403

11. SUPPLEMENTARY NOTES

Responsible person, Hsiao C. Kao, organization code 5860, (216) 433-5866.

12a. DISTRIBUTION/AVAILABILITY STATEMENT

Unclassified - Unlimited
Subject Categories: 02 and 71 Distribution: Nonstandard

This publication is available from the NASA Center for AeroSpace Information, (301) 621-0390.

12b. DISTRIBUTION CODE

13. ABSTRACT ***(Maximum 200 words)***

The problem of sound generation by vortices interacting with an arbitrary body in a low-speed flow has been investigated by the method of matched asymptotic expansions. For the purpose of this report, it is convenient to divide the problem into three parts. In the first part the mechanism of the vortex/body interaction, which is essentially the inner solution in the inner region, is examined. The trajectories for a system of vortices rotating about their centroid are found to undergo enormous changes after interaction; from this, some interesting properties emerged. In the second part, the problem is formulated, the outer solution is found, matching is implemented, and solutions for acoustic pressure are obtained. In the third part, Fourier integrals are evaluated and predicated results presented. An examination of these results reveals the following: (a) the background noise can be either augmented or attenuated by a body after interaction, (b) sound generated by vortex/body interaction obeys a scaling factor, (c) sound intensity can be reduced substantially by positioning the vortex system in the "favorable" side of the body instead of the "unfavorable" side, and (d) acoustic radiation from vortex/bluff-body interaction is less than that from vortex/airfoil interaction under most circumstances.

14. SUBJECT TERMS

Vortex/body interaction; Sound generation; Asymptotic matching; Discrete Fourier transform

15. NUMBER OF PAGES

38

16. PRICE CODE

A03

17. SECURITY CLASSIFICATION OF REPORT	18. SECURITY CLASSIFICATION OF THIS PAGE	19. SECURITY CLASSIFICATION OF ABSTRACT	20. LIMITATION OF ABSTRACT
Unclassified	Unclassified	Unclassified	